Thesis for the Degree of Master

Design of the Silicon Tungsten Calorimeter Prototype for e^+e^- International Linear Collider

by
Sung Kyun Park
Department of Physics

Graduate School
Korea University

February, 2005

Abstract

We have made the silicon-tungsten calorimeter prototype for the future e^+e^- International Linear Collider and carried out the beam test at CERN. We have also analyzed the data by developing root-based programs. Therefore the energy solution as a result of the analysis is $31.3\% \pm 0.5\%$. Through this research, we accumulate the technic about the calorimeter and after improving our prototype issue, we are to plan to set up next prototype design for the future e^+e^- ILC.

Contents

List of Figures

List of Tables

Chapter 1

Introduction

The highest energy ever reached at e^+e^- colliders was about 210 GeV, achieved by LEP (Large Electron Position Collider) at CERN, Geneva. Operation of LEP was terminated in 2000. The current energy frontier machine is TEVATRON at Fermilab, USA. This is a $p\bar{p}$ collider with a center-of-mass energy (E_{CM}) of 1.96 TeV. At CERN, a new pp collider, LHC, is under construction. Its center-of-mass energy will be 14 TeV. Experiments are scheduled to start in 2007.

International Linear Collider(ILC) would be also an energy frontier e^+e^- collider for next question of high energy physics . Its major element is a series of linear accelerators (linac). The initial goal of the ILC project is to perform experiments at an e^+e^- center-of-mass energy of up to 500 GeV, with a provision for further upgrades beyond 1 TeV. This energy is to simulate the early Universe, 10^{-12} second after the Big Bang, with a temperature of 10^{16} K, which corresponds to being able to probe structure as tiny as 10^{-18} m given in Table 1.1. And this energy is the proper level to find and study the Higgs boson.

The reason that we must construct ILC in the future is to have an experiment of e^+e^- collision at the range of higher energy than the energy achieved by LEP. But it was recognized that the energy of a circular machine is practically limited at the LEP energy (210 GeV) due to beam energy loss by synchrotron radiation. The concept of a linear collider was proposed [2] to circumvent this limitation. ILC is an e^+e^- linear collider which goes well

Temperature (Kelvin)	Energy (GeV)	Time
2.7	2.3×10^{-13}	12×10^{9}y
15	10^{-12}	10^{9}y
3000	3×10^{-10}	3×10^{5}y
10^{9}	10^{-4}	10^{2}s
10^{12}	10^{-1}	10^{-5}s
10^{15}	10^{2}	10^{-10}s
10^{32}	10^{19}	10^{-44}s

Table 1.1: Energy and Temperature during the early Universe

beyond the energies that could be researched by LEP.

And there are several advantages in e^+e^- collision compared with pp collisions, even though the beam energy of ILC is lower than that of LHC. First, at e^+e^- collider, the entire collision energy can be utilized for the physics process of interest. On the other hand, only a part of the energy can be put into the corresponding subprocess at LHC, because the proton is a composite particle made of quarks and gluons. Second, at hadron colliders the background is very severe, so the techniques for analysis of data obtained at their experiments become considerably complex. On the other hand, in the clean environment of e^+e^- collisions, the detector performance can be maximized so as to fully meet the requirements for physics analysis.

History shows that the concurrent running of energy-frontier e^+e^- colliders and hadron colliders is of vital importance. LHC, taking advantage of its higher energy reach, will scan and discover distinctive signatures of new physics. However, ILC, through precision measurements, will clarify and establish new principles of Nature behind the current physics. Both relations are complementary to each other.

The main physics at ILC is a precision study on the Higgs boson. At the machine with a center-of-mass energy of 300-500 GeV and an integrated luminosity of $500fb^{-1}$, O(10^5) Higgs bosons can be produced if the Higgs mass is smaller than 200GeV. Hence, ILC will be called a Higgs factory. By measuring the Higgs couplings to gauge bosons and fermions as well as the Higgs-self coupling, we would be able to reveal the structure of the Higgs

boson.

In addition, a TeV-scale LC may enable us to explore the heavy Higgs boson beyond the standard model(SM).[3] And an unambiguously known physics threshold exists for top-quark pair[5] production at the center-of-mass energy of 350 GeV. The top quark is the heaviest elementary particle observed to data, whose production and decays have not been fully experimentally studied. Therefore the first phase of the physics at ILC should be able to explore the light Higgs boson and the top-quark threshold. And after upgrades beyond 1TeV, ILC might be discover experimentally the existence of super-partner particles for electrons and quarks, s-electrons($\widetilde{e}$) and s-quarks($\widetilde{q}$), which have been predicted by supersymmetric theories.[4]

Table 1.2 lists the research potentials expected for LHC and ILC about each physics area such as the study on the light and heavy Higgs boson, the study of top-quark and the study of super-partner particles and so forth. And we can again know the relation of LHC and ILC is not competitive but complementary to each other.

The principal requirements for the electromagnetic calorimeter in a ILC experiment may be summarized as follows:[6]

- Good energy resolution for photons and electrons; needed for example for e/π separation and for the identification of H $\rightarrow\gamma\gamma$ events.
- Excellent transverse spatial resolution, in order to separate particles in jets and make energy flow measurements.
- Good longitudinal segmentation as an aid to e/π separation.
- The ability to identify non-pointing photons; for example in the gauge-mediated SUSY breaking scenario where a long-lived neutralino may decay to a photon and a stable gravitino: $\widetilde{\chi_1^0} \rightarrow \gamma\widetilde{G}$.
- Excellent hermeticity.
- Good time resolution, to avoid pile-up from particles originating from other bunch crossings.
- Compact, so that the calorimetry can be placed inside the magnet coil without prodigious cost.

Si-W electromagnetic calorimeter might provide a good solution for these purpose.

In this study we have studied the calorimetry and made the prototype for the Si-W calorimeter and carried out the beam test at the CERN in 2004. In this thesis, we take a look at the Higgs mechanism in Chapter2. we review the EM showers process briefly in Chap 3. In Chap 4 the design development process of mechanical prototype is described, and in chap 5 our development process of the analysis code and the analysis result is mentioned as compared with the simulation results and in chap 6 we are to summarize the result about whether how good calorimeter our prototype is.

	LHC	ILC	
		500 GeV	1 TeV
Light Higgs boson (120-140 GeV)			
Detection	◯	◯	-
Width(Γ_H)	△	◯	-
J^P	△	◯	-
Coupling ($_{gVVH}$,$Y_{f\bar{f}H}$)	◯	⋆	-
Top Yukawa C.C ($Y_{t\bar{t}H}$)	△	×	◯
Self-coupling($_{HHH}$)	×	△	◯
500 GeV SM Higgs boson			
Detection	◯	×	◯
Top quark			
Δm_t	**$\sim$ 1 GeV**	100 MeV	-
Width (Γ_t)	×	a few %	-
Supersymmetry			
Squark mass reach	**2.5 TeV**	$\sqrt{s}/2$	
Slepton/Chargion/Neutralino	**Cascade decay**	Pair production	
Mass measurement	◯	⋆	
Proving SUSY (Spin, Coupling)	×	⋆	
Testing SUSY breaking model	◯	◯	
MSSM Heavy Higgs	**high tanβ**	$\sqrt{s}/2$	
Indirec constraint			
on SUSY parameters	△	◯	◯
Large Extra Dimension			
KK gravition	◯	△	◯
Black hole production	◯	×	△
(Z, KK graviton of RS model,	**Direct production**	Contact interaction	
KK mode of W and Z, etc.			
Mass reach	◯	◯	⋆

Table 1.2: Research potentials expected for the LHC and ILC. LHC with an integrated luminosity of $\sim$100fb^{-1} and a 500 GeV e^+e^- linear collider with $\sim$500fb^{-1} are compared. The merits of the energy extension of the linear collider to 1 TeV are shown in the column of 1 TeV LC. star, excellent; circle, good; triangle, fair; cross, not useful. - means that this category is already fully coved at the 500 GeV e^+e^- linear collider.

Chapter 2

Higgs Boson

In the Standard Model, all particles are massless if there is no symmetry breaking in the electroweak sector. A spin-zero field called Higgs field is introduced to trigger electroweak symmetry breaking. This field is assumed to fill everywhere in the Universe, and its condensation in the vacuum state is responsible for the breakdown of the electroweak symmetry. The Higgs boson is a physical excitation mode of the Higgs field. However, it has not been found experimentally up to now. In order to test the electroweak symmetry breaking and mass generation mechanism, we should be able to find and study the Higgs boson with the aid of ILC.

In this chapter, we will consider spontaneous symmetry breaking [7] and mass generation mechanism briefly.

2.1 Spontaneous symmetry breaking

The general Lagrangian for the scalar field which interacts with each other would be

$$L = T - V = \frac{1}{2}(\partial_\mu \phi)^2 - \frac{1}{2}\mu^2\phi^2 - \frac{1}{4}\lambda\phi^4 \tag{2.1}$$

where μ is mass of scalar particle, and λ is a dimensionless constant, representing the coupling of the 4-boson vertex. The minimum value of V occurs

at $\phi = \phi_{min}$, when $\partial V/\partial\phi = 0$ or

$$\phi(\mu^2 + \lambda\phi^2) = 0 \tag{2.2}$$

If $\mu^2 > 0$, then $\phi = \phi_{\min}$ when $\phi = 0$; this is the normal situation for the lowest energy vacuum state with V = 0. However, if $\mu^2 < 0$,

$$\phi = \phi_{min} \text{ when } \phi = \pm v = \pm\sqrt{\frac{-\mu^2}{\lambda}} \tag{2.3}$$

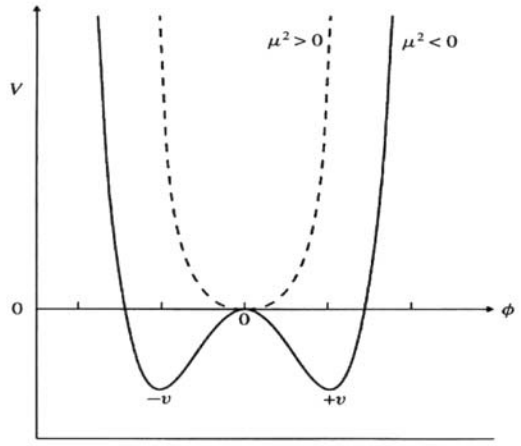

Figure 2.1: Plot of the potential V in (2.1) as a function of a one-dimensional scalar field ϕ for the two cases $\mu^2 > 0$ and $\mu^2 < 0$.

Here the lowest energy state has finite ϕ , with $V = \mu^4/4\lambda$, so that V is everywhere a non-zero constant. The quantity v is called the vacuum expectation value of the scalar boson field ϕ. Figure 2.1 describes V as a function of ϕ, both for $\mu^2 > 0$ and $\mu^2 < 0$ modes. In either case a symmetric curve results, but for $\mu^2 < 0$ there are two minima, $\phi_{min} = v$ and $-v$. In weak interactions, we are concerned with evaluating small perturbation about the energy minimum, so that we should expand the field variable ϕ, not about zero(unstable solution) but the chosen vacuum at absolute minimum v or -v, i.e.

$$\phi = v + \sigma(x) \tag{2.4}$$

where $\sigma(x)$ is the value of the field over and above the constant and uniform value, v. Substituting this into (2.1) we obtain

$$L = \frac{1}{2}(\partial_\mu\sigma)^2 - (\lambda v^2\sigma^2 + \lambda v\sigma^3 + \frac{1}{4}\sigma^4) + \frac{1}{4}\lambda v^4 \tag{2.5}$$

The last term is a constant term of the Lagrangian. This term can be ignored since the zero level of the potential can be refined in the given Lagrangian. and the term with σ^2 has the correct sign so it can be interpreted as a mass term. This Lagrangian represents a particle with mass

$$m = \sqrt{2\lambda v^2} = \sqrt{-2\mu^2} \tag{2.6}$$

and they interact with themselves with $\lambda v\sigma^3 + \frac{1}{4}\sigma^4$.

There is no trace of the reflection symmetry $\phi \rightarrow -\phi$ in equation(2.5). A memory of it is preserved in the σ^3 interaction term but not in an obvious way. Because the symmetry was broken, in a sense, when a specific vacuum was chose the vacuum does not have the symmetry of the original Lagrangian, so the solution do not. When this occurs it called spontaneous symmetry breaking. This procedure is the basic idea of the Higgs mechanism.

2.2 Higgs mechanism

In Higgs mechanism, it is needed to construct the proper Lagrangian with SU(2) × U(1) invariant Yukawa coupling and substitute the mass eigenstate field of bosons or fermions for mass generation. Then one will have the quadratic fields terms, multiplied by the Higgs vacuum term v^2, which as in (2.5) will be associated with the masses of these particles. In fact this term leads to relations for the squares of the boson or fermion masses.

The mass formula are given by $M_W = \frac{gv}{2}$, $M_Z = \frac{v}{2}\sqrt{g^2 + g'^2}$, $M_f = \frac{y_f}{2}v$, and $M_H = \sqrt{\lambda}v$, where $v \simeq 246$ GeV is the Higgs vacuum expectation value, g and g' are SU(2) and U(1) gauge coupling constants, and y_f is the Yukawa coupling constant for the fermion *f*. These expressions imply that a particle mass is determined by the strength of its interaction to the Higgs field. Therefore the measurement of the coupling constants, which relate to the Higgs boson, is an important check of the mass generation mechanism in the SM.

The formula of Higgs mass, $M_H = \sqrt{\lambda}v$ suggests that the mass of the

Higgs boson reflects the strength of the electroweak symmetry breaking dynamics since λ represents interactions of unknown strength. Therefore the heavy Higgs boson implies the strongly-interacting dynamics and the light Higgs boson is consistent with the weakly interacting scenario such as grand unified theory(GUT) or supersymmetric unified models.

In the e^+e^- collision, the Higgs boson is produced by two different processes, one by the Higgs-strahlung process, $e^+e^- \to Z^* \to ZH$, and the other by the weak boson fusion reactions, WW-fusion($e^+e^- \to \nu\bar{\nu}W^*W^* \to \nu\bar{\nu}H$) and ZZ-fusion($e^+e^- \to e^+e^-Z^*Z^* \to e^+e^-H$). The Feynman diagrams of Higgs production are shown in Fig 2.2. The Higgs-strahlung is dominant process at lower energies while the fusion processes become significant at higher energy for light Higgs.

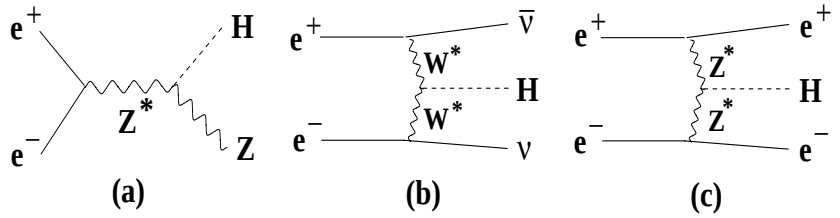

Figure 2.2: Feynman diagrams of CP-even Higgs production from e^+e^- collision. (a)Higgs-strahlung(Bijörken) ZH production, (b)WW-fusion and (c)ZZ-fusion.

Since self coupling constant, λ is unknown at present, the value of the Standard Model Higgs mass is not known exactly. So we are able to guess the Higgs mass by the use of the theoretical constraints. In the case of light Higgs boson, assuming that the SM is valid up to the Planck scale (10^{19} GeV), the mass of the Higgs boson is theoretically constrained in the range between 135 GeV and 180GeV shown in Figure 2.3. In the two Higgs doublet model (THDM), the mass of the lightest CP-even Higgs boson(m_h) is expected in the region between 100GeV and 180GeV for the Planck scale in the decoupling regime where only one Higgs boson is light [8]. In the minimal supersymmetrical standard model (MSSM), we can derive the upper bound of m_h(130 GeV) without reference to the cut-off scale. [9] For the extended SUSY model with the gauge singlet field(NMSSM),the bound is about 150GeV if we assume that the theory is valid up to the GUT scale.[10]

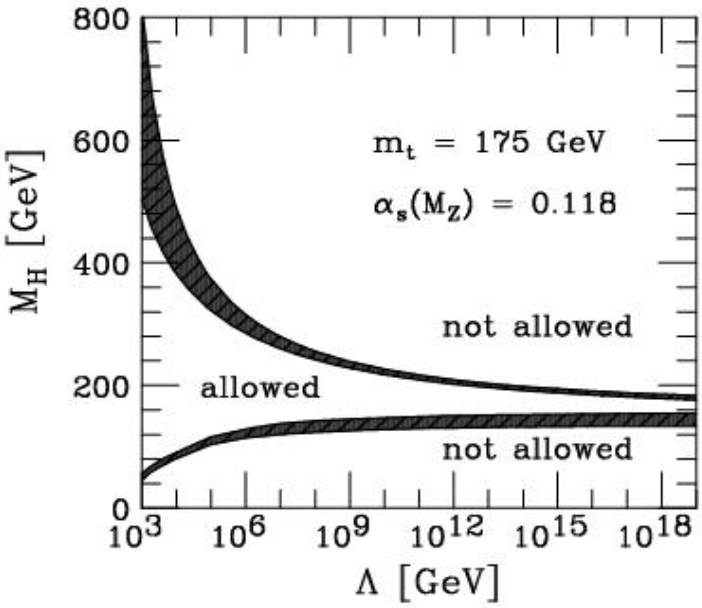

Figure 2.3: Summary of the uncertainties connected to the bounds on M_H

Chapter 3

Electromagnetic Shower Process

3.1 The Electromagnetic interaction

The well known energy-loss mechanism contributing to the absorption process is the Electromagnetic (EM) interaction experienced by charged particles traversing matter. And the EM interaction is able to take place in many ways.

- The particles ionize the medium, if their energy is at least sufficient to release the atomic electrons from the Coulomb fields generated by the atomic nuclei.
- Charged particle may excite atoms or molecules without ionizing them. The deexcitation from these metastable states may yield scintillation or light, which is also fruitfully used as a source of calorimeter signal.
- Charged particles traveling faster than the speed of light characteristic for the traversed medium lose energy by emitting $\check{C}$erenkov radiation.
- At high energies, energetic knock-on electrons (δ-rays) are produced.
- At high energies,bremsstrahlung is generated.
- At very high energies, the EM interaction may induce nuclear reactions.

In this process, the principal source of energy loss by electrons and positrons is bremsstrahlung. In their passage through matter, electrons and positrons radiate photons as a result of the Coulomb interaction with the electric fields generated by the atomic nuclei. The energy spectrum of these photons falls off as $1/E$. And the electrons or positrons themselves undergo a change in direction. This is called multiple or Coulomb scattering. This deviation depend on the angle and the energy of the emitted photons, which in turn resulted to the strength of the Coulomb field, namely on the absorber material.

3.1.1 Photoelectric effect

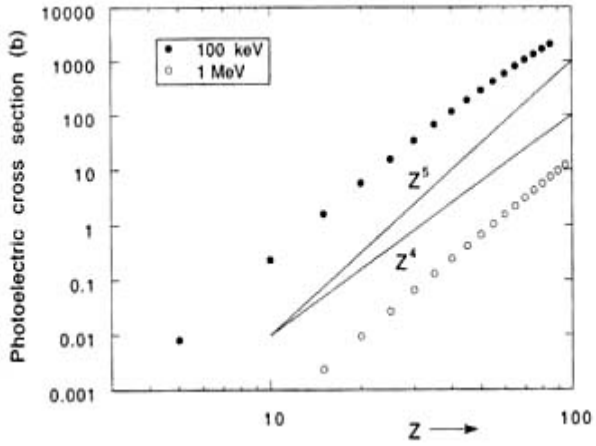

Figure 3.1: The cross section for the photoelectric effect.[11]

At low energies, this is the most likely process to occur. In this process, an atom absorbs the photon and emits an electron. Atoms left in an excited states return to the ground states by the emission of Auger electrons or X-rays. The photoelectric cross section is dependent on the available number of electrons, and on the Z value of the absorber material. This is illustrated in Figure 3.1. Also the photoelectric cross section varies with the photon energy as E^{-3}, so that this process rapidly loses its importance as the energy increases.

3.1.2 Rayleigh scattering

This process is called coherent scattering and important at low energies. The photon deflected by the atomic electrons does not lose energy. Therefore Rayleigh scattering affects the spatial distribution of the energy deposition. but it does not contribute to the energy deposition process itself.

3.1.3 Compton scattering

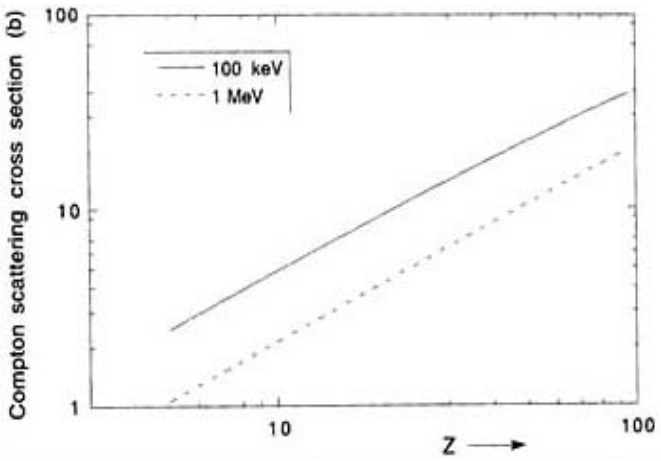

Figure 3.2: The cross section for Compton scattering.[11]

In Compton scattering, photons are scattered by atomic electrons with transfer of momentum and energy to the struck electron sufficient to put this electron in an unbound state. Figure 3.2 shows that the Compton cross section is almost proportional to Z, namely proportional to the number of target electron in the nucei. As for the photoelectric effect, the cross section for Compton scattering decreases with increasing photon energy. so, above a certain threshold energy, Compton scattering becomes more likely than photoelectric absorption.

3.1.4 Pair production

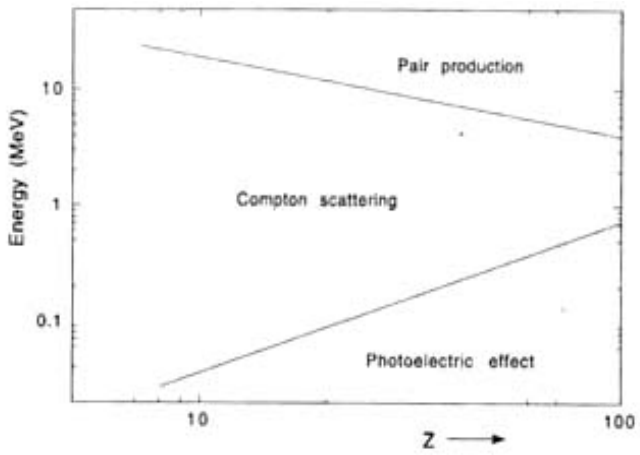

Figure 3.3: The energy domains between photoelectric effect, Compton scattering and pair production.[11]

At energies larger than twice the electron rest mass, a photon may create an electron-positron pair in the electromagnetic field of a charged particle such as atomic nuclei. These particles produce bremsstrahlung radiation as well as ionization along their paths. The electron is eventually absorbed by an ion, while the positron annihilates with an electron. In latter process, two new photons are produced, each with an energy of 511 keV, the electron rest mass energy, if the annihilation takes place when the positron has come to rest. The cross section for pair production rises with energy and reaches an asymptotic value at very high energies (> 1 GeV). This cross section is related to the radiation length of the absorber material. In Figure 3.3 the photoelectric effect dominates at low energies. Compton scattering is the process of choice in some intermediate energy regime. The higher the Z value of the absorber, the more limited the role of Compton scattering in the em absorption process.

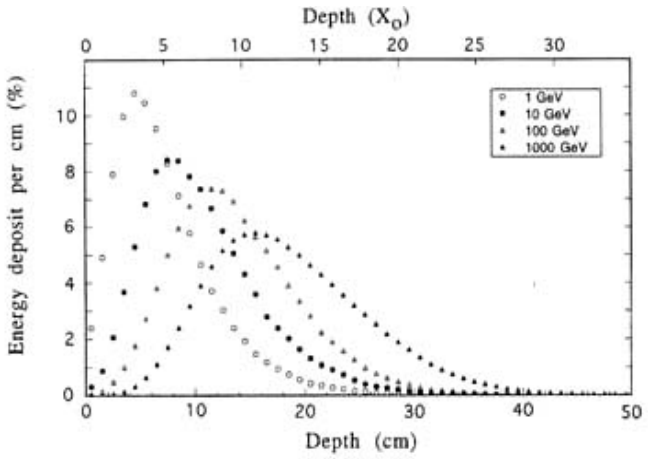

Figure 3.4: The energy deposit as a function of depth, for 1, 10, 100, and 1000GeV electron showers developing in a block of copper. [11]

3.2 Electromagnetic shower

There is one more, crucial, mechanism that determines the absorption characteristics of electromagnetically interacting particles in the GeV domain: bremsstrahlung, the radiation of large numbers of photons as a result of the interaction between the high-energy electrons and positrons and the nuclear Coulomb fields. So we are able to think bremsstrahlung is by far the main source of energy loss by high-energy electrons and positrons.

A primary, multi-GeV electron may radiate thousands of photons on its way through the detector material. The overwhelming majority of these photons are very soft, and are absorbed through Compton scattering and the photoelectric effect. The photons carrying higher energy than 5-10 MeV create e^+e^- pairs. The electrons and positrons generated in these processes may in turn lose their energy by radiating more photons, which may create more electron-positron pairs. The result is a shower phenomenon that may consist of thousands of different particles; electrons, positrons and photons.

The shower energy is deposited in the absorbed material through ionization by the numerous electrons and positrons. Because of the multiplication mechanism described above, the number of electrons and positrons, and thus

the amount of energy deposited in a slice of given thickness , initially increases as the shower develop with increasing shower depth.

However, as the shower develops, the average energy of the shower particles decreases, and at some point no further multiplication takes place. The depth at which this occurs is called the shower maximum. Beyond this depth, the shower photons are, on average, more likely to produce one electron in their inter compton and photoelectric interactions than an electron-position pair. And the electrons and positrons are, again on average, more likely to lose their energy through ionization of the absorber medium than to produce new photons through radiation. Beyond the shower maximum, the number of shower particles, and thus the energy deposited in a detector slice of given thickness, gradually decreases. All these aspects are illustrated in Figure 3.4. And we are able to find that the higher the initial energy of the showering particle, the longer the particle multiplication phase continues.

Since the EM shower development is primarily determined by the electron density in the absorbed medium,in general, it is to some extent possible to describe the shower characteristics in a material-independent way. The units that are frequently used to describe the characteristic shower dimensions are the radiation length (X_0) for the longitudinal development and the *Molière radius* (ρ_M) for the transversal development.

3.2.1 The radiation length

The radiation length is defined as the distance over which a high-energy ($\gg 1GeV$) electron or positron loses, on average, 63.2 % (1-e^{-1}) of its energy to bremsstrahlung. High-energy electrons lose typically the same fraction of the energy in 18 cm of water (0.5 X_0)as in 2.8 mm of lead (0.5 X_0).

The asymptotic cross section for photon interactions is related to X_0 [12] as

$$\sigma(E \to \infty) = \frac{7}{9}\frac{A}{N_A X_0} \tag{3.1}$$

in which X_0 is expressed in gcm^{-2} and the ratio of Avogadro's number (N_A) and the atomic weight(A) denotes the number of atoms per gram of material. This implies the mean free path of very-high-energy photons equals to $\frac{9}{7}X_0$.

For approximate calculations,which are accurate to within 3 %, the Particle Data Group recommends the following expression:[13]

$$X_0 = \frac{716.4 \text{ g cm}^{-2} A}{Z(Z+1)\ln(287/\sqrt{Z}} \tag{3.2}$$

And Table 3.1 illustrate the atomic properties of materials including the radiation length.

Material	Z	A	Z/A	$dE/dx\|_{min}$ $\frac{MeV}{g/cm^2}$	Radiation length g/cm^2	cm
$H_2 gas$	1	1.00794	0.99212	(4.103)	61.28	731000
N_2	7	14.00674	0.49954	(1.825)	37.99	47.1
O_2	8	15.9994	0.50002	(1.801)	34.24	30.0
Al	13	26.9815	0.48181	1.615	24.01	8.9
Si	14	28.0855	0.49848	1.664	21.82	9.36
W	74	183.84	0.40250	1.145	6.76	0.35

Table 3.1: Atomic Properties of Materials.

The radiation length for a mixture of different material can be calculated from the following formula:[14]

$$\frac{1}{X_0} = \sum_i \frac{V_i}{X_i} \tag{3.3}$$

V_i and X_i are the fraction by volume and the radiation length of the ith component of the mixture.

3.2.2 The Molière radius

The Molière radius is frequently used to describe the transverse development of electromagnetic showers in an approximately material independent way. It is defined in terms of the radiation length X_0 and the critical energy E_c, as follows:[15]

$$\rho_M = E_s \frac{X_0}{E_c} \tag{3.4}$$

The scale energy E_s, defined as $m_e c^2\sqrt{4\pi/\alpha}$, equals 21.2 MeV on average, 90 % of the shower energy is deposited in a cylinder with radious ρ_M around the shower axis. We define the critical energy E_c as the energy at which the average energy loses from radiation processes equal those from ionization. And we adopt the following expressions for the critical energy:[16]

for materials in the solid or liquid phase

$$E_c = \frac{610 \text{ MeV}}{Z + 1.24} \tag{3.5}$$

for gases

$$E_c = \frac{710 \text{ MeV}}{Z + 0.92} \tag{3.6}$$

The Molière radius of compound of different elements may be calculated in the same way as the radiation length for such mixture or compound was obtained. And the Molière radius is much less Z dependent than the radiation length. So the radiation length scales in first approximation with A/Z^2. If we assume that A is proportional to Z, which is roughly true, the radiation length decreases with increasing Z like $1/Z$.

3.3 Electromagnetic shower profiles

In Figure 3.5 we exhibit the fact that as Z increase, the shower maximum shifts to greater depth and the shower profiles decay more slowly beyond the shower maximum. And the number of positrons strongly increase with the Z value of the absorber material. This is due to the fact that in high-Z materials, shower particle multiplication, namely the production of e^+e^- pairs by photons and the emission of bremsstrahlung photons by these charged shower particles, continues down to much lower energies than in low-Z materials. As the shower develops, the average energy of the shower particles decreases with each new generation. The shower maximum is reached when the average energy of the shower particles equals to the critical energy.

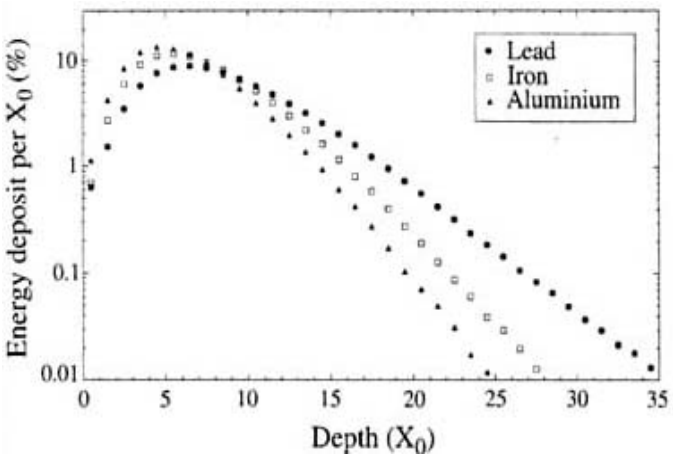

Figure 3.5: Energy deposit as a function of depth. X_0 [17]

The lateral spread of electromagnetic shower is caused by two effects. First, electrons and positrons move away from the shower axis due to multiple scattering. Second, photons and electrons produced in isotropic processes move away from the shower axis. Also bremsstrahlung photons emitted by electrons that travel at a considerable angle with respect to the shower axis may contribute to this effect. The first process dominates in the early stages of the shower development, while the second process is predominant beyond the shower maximum, particularly in high-Z absorber media.

Chapter 4

Design and Assembly of Mechanical Structure

The electromagnetic(EM) calorimeter of the future e^+e^- Linear Collider must have not only good energy resolution but also compact size since this is to be placed inside the magnetic coil. Therefore the size of the EM calorimeter is most important parameter for a silicon-tungsten(Si-W) calorimeter to be confirmed as the EM calorimeter of the future e^+e^- Linear Collider.

4.1 Design of Mechanical Structure

4.1.1 Size of Mechanical Structure

At the initial stage of design about the prototype of mechanical structure, the most considerable parameter was the size of silicon sense. Since this sensor is not made for our experiment exclusively, the sense shape is not a square, the sensor form of the most detectors [18], but a rectangle. Therefore the shape of our calorimeter is not the square. The size of a silicon sense is 58 mm $\times$ 65 mm. And since a side 1 mm is the dead zone according to the Figure 4.1, the size of an active area in the sensor is 57 mm $\times$ 64 mm. Since We have planed to set up four sensors on a layer, there is the dead zone between sensors in the active area of a layer. Because the dead zone isn't able to detect particles, to decrease the area of the dead zone in the

active area when we are to arrange four sensors in our calorimeter is one of an important design specification. The Figure 4.1 illustrates the front side and the back side of our sensor.

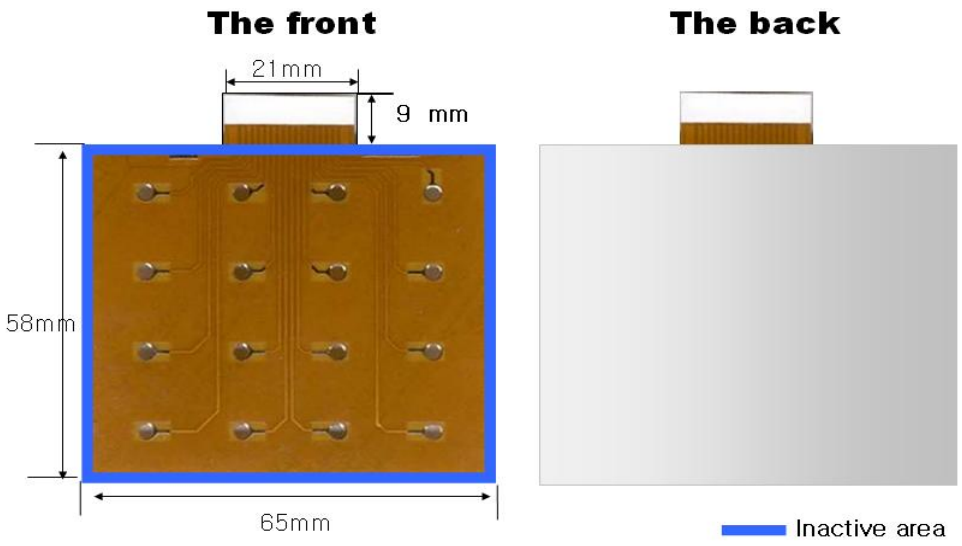

Figure 4.1: Silicon sensor

Figure 4.2 shows the real arrangement of four sensors on a layer concretely. At x axis, the silicon sensor is separated with the intervals of 1mm and at y axis, the silicon sensor is overlapped with the intervals of 1mm. So the active area of four sensors arrangement is 131 mm $\times$ 115 mm as referred in Figure 4.2. The reason why such an complex arrangement is used is that there is high voltage on the sensor operated. If the nearest sensors is connected each other, they will be able to have a damage. Therefore, we need to have a gap of about 1 mm between sensors at the x axis. But at y axis, we don't consider this gap since the nearest sensor is not connected as seen in the Figure 4.3. The back of the sensor is arranged in the real experiment in the course of adapting the sensor for our experiment.

The tungsten size is same with the active area of four sensors arrangement; 131 mm $\times$ 115 mm. Since the tungsten is very hard, we can not manipulate it easily and especially find out tungsten merchandise in a plate

form made in Korea, which function as a medium to happen the EM shower. Therefore we have imported these from China. As we can use these at the another experiments, we reduce the size one-fourth of the active area manageable to recycle it. Therefore the size of tungsten ordered is 65.5 mm $\times$ 57.5mm.

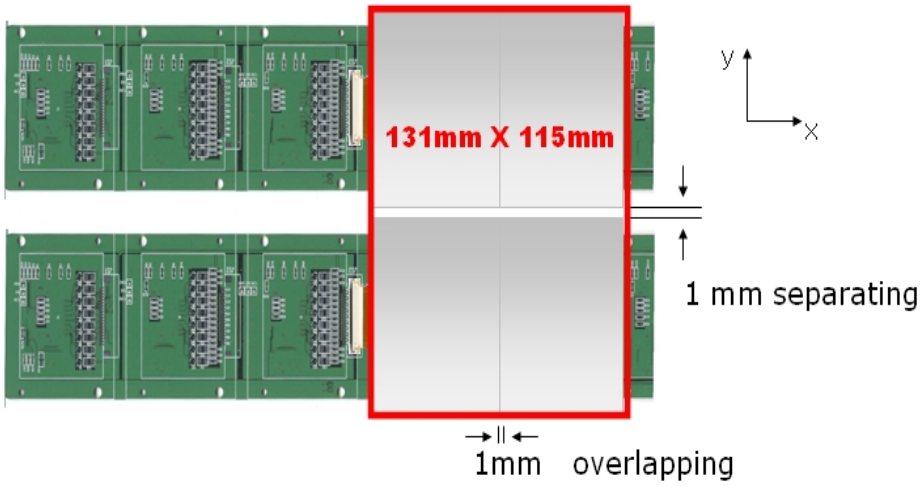

Figure 4.2: The active area of four sensors on a layer

Until now we have considered the size of the width and length of the active area of our detector. The next step is the thickness of our detector. we must consider two points remarkably; a thickness of the tungsten and electronics readout system. We have decided the thickness of Tungsten by radiation length. The tungsten we have used for our experiment is that purity was 99.9 % and the radiation length is 3.5mm.

In general the radiation length has something to do with a longitudinal shower development. Namely an electron of energy ($E \gg E_c$) gives one electron and one photon, each of energy $E/2$ after one radiation length X_0. one photon of energy E will give an electron-positron pair, each particles having energy $E/2$. After t radiation lengths there will be 2^t particles, each having energy E=$E_0 2^{-t}$ where E_0 was the energy of the initial particle. Such a shower would continue to grow until $E = E_c$ is reached and then the number of particle would be $N_{MAX} = E_0/E_c$. Since our radiation lengths is 20

X_0, the maximum number of particles will become 2^{20} particles. We know the radiation length of each material from Particle Data Book(PDA)[19]. And we will be able to find the radiation length for a mixture of different materials in equation (3.3). Therefore the effective radiation length of our detector is 14.91 mm.

Next, we look over an electronics readout system of out calorimeter. The silicon sensor play the eye's role in out detector. And we need something to control the silicon sensor. The analog board has this role. The analog board consist of resistor,capacitor,connector,CR 1.4 chip and silicon sensor on the PCB. A core of the analog board is a CR 1.4 chip which controls and amplifies the signal captured by the silicon sensor. A simplified schematic about the profiles of our detector is illustrated in Figure 4.3.

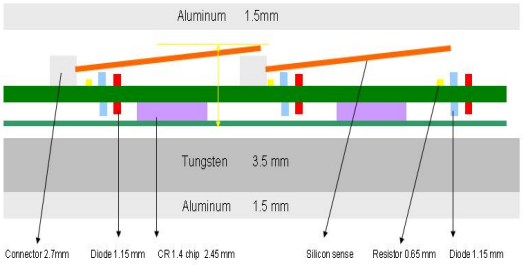

Figure 4.3: An Electronics Readout System

The thickness of the analog board which includes the sensor, the chip, and others at the last detector design is 10 mm. and this is more thick than the design of Calice, which is an European R&D group of a Silicon Tungsten Calorimeter. The next design of the Calorimeter of our group try to reduce the thickness of the electronics readout system. The thickness of each layer of our detector is 15 mm now. When we set up 20 layers, the thickness is 300 mm. We are also able to think about the effective Molière radius of our detector using equation (3.3)(3.4). Therefore the effective Molière radius of our detector is 27.33 mm.

As outside Electromagnetic wave can affect our system, we need something which can protect the outside influence. Figure 4.4 represents shielding

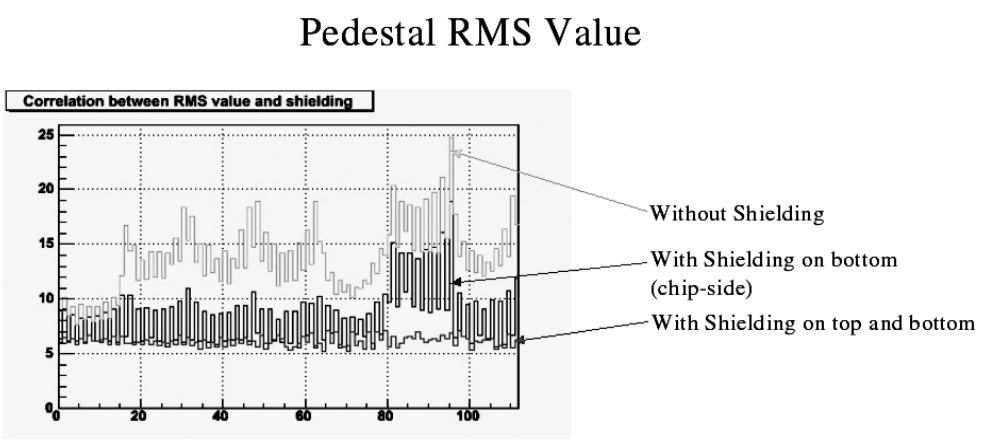

Figure 4.4: The relation between RMS and shielding

is very effective. namely increasing the shielding decrease the value of RMS as shown at Figure 4,4. Because of the structure of our electronics system, we can not shield on bottom and top so we shielded on bottom only.

4.1.2 Design of Mechanical Structure

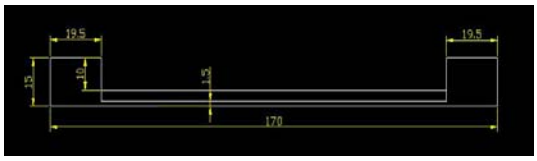

Figure 4.5: CAD profile of Mechanical structure

Figure 4.5 is the profile of our Mechanical Support Structure (MSS) drawn by CAD. We selected Aluminum as its material, which was very tender enough to be manipulated easily. At the first stage of making the structure of MSS, the thickness of the ground of MSS is very thin, 1.5mm. So we are not able to use the method digging out from the Aluminum mass of the size 150mm×170mm×15mm. If we do this method, we may not make the ground flat.

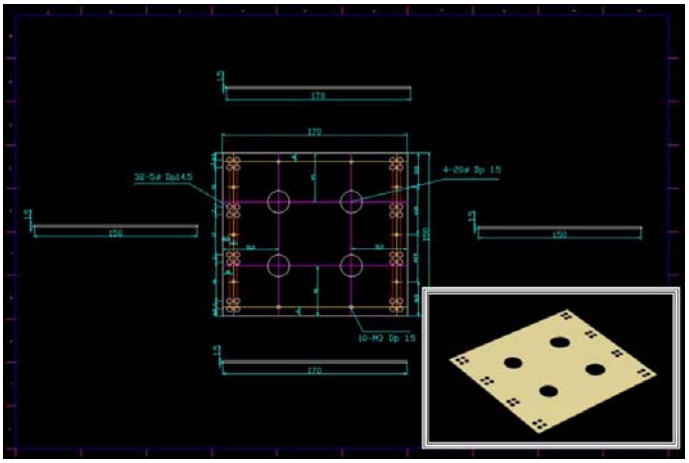

Figure 4.6: Mechanical Supported Structure Type1 150mm×170mm×1.5mm

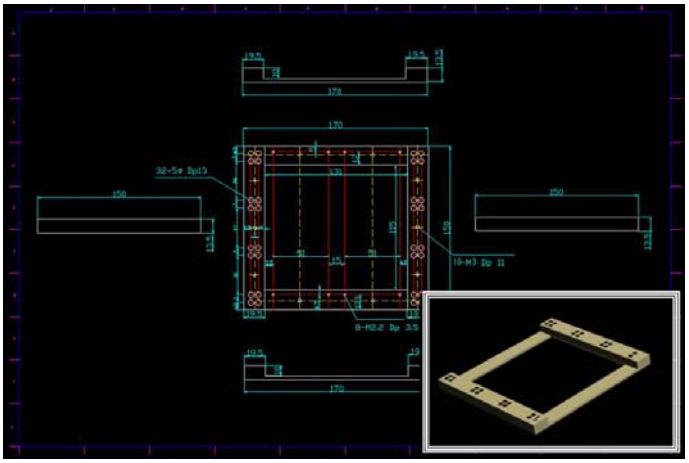

Figure 4.7: Mechanical Supported Structure Type2 150mm×170mm×13.5mm

So we have tried to find a lot of another methods which we have made MSS by. Finally we find out the method, making two parts,MSS Type 1 and MSS Type 2, and assembling them. And in this method we will be able to make the ground of MSS flat. MSS Type 1 is the aluminum plate whose size is 150mm×170mm×1.5mm in Figure 4.6. And MSS Type 2 is the complex

structure of an aluminum whose size is 150mm×170mm×13.5mm in Figure 4.7. The attachment is perfectly achieved by using a bolt and a nut. And then we have inserted the tungsten plate into MSS. And the left side of Figure 4.8 illustrate this process. After we complete to set up MSS, we find some gap plates which can nearly not be identified by our eyes. If we are to shoot the beam in the direction of the center, this gaps will be a large part of the experiment error.

In the fundamental Mechanical Support Structure (FMSS) which consist of MSS Type1 and MSS Type2 and four tungsten, we will be able to find two kinds of circles whose size are different. The right side of Figure 4.8 shows these rings.. The radius of large circle is 10mm and that of small circle is 2.5mm.

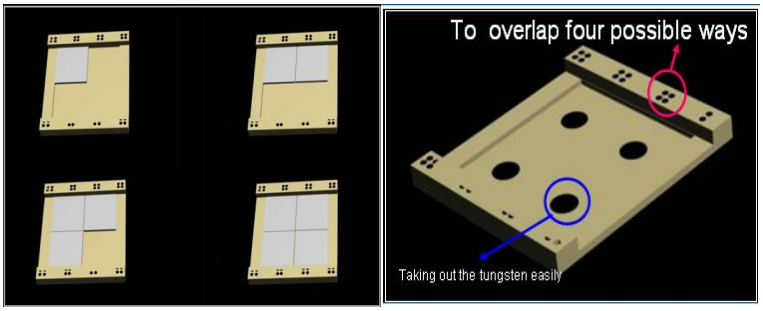

Figure 4.8: Fundamental Mechanical Supported Structure(FMSS)

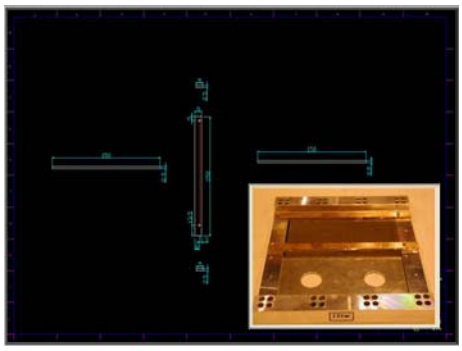

Figure 4.9: The bar design

Two rings have the different functions. The role of the large one is to pull out the tungsten, which is inserted tightly, from FMSS easily. The role of the small one is the hole to put in the support, a pole. Because the screw hole of PCB was apart from the screw hole of the MSS, we have needed something connecting between the screw holes of PCB and MSS. So we have made the bar whose size is 150mm×9mm×2.5mm. This is mounting both the tungsten and PCB in Figure 4.9. The fundamental Mechanical Supported Structure(FMSS) is made by the assembling method as shown in Figure 4.9.

4.1.3 Assembly

From now we must have assembled mechanic part(FMSS) and electronic part to make a layer of our calorimeter. We have set up an analog board and the silicon sensor on the MSS. The left side of Figure 4.10 have represented this process. And the right side of Figure 4.10 was to show the real appearance of our calorimeter accumulated after completing the assembly of each layer.

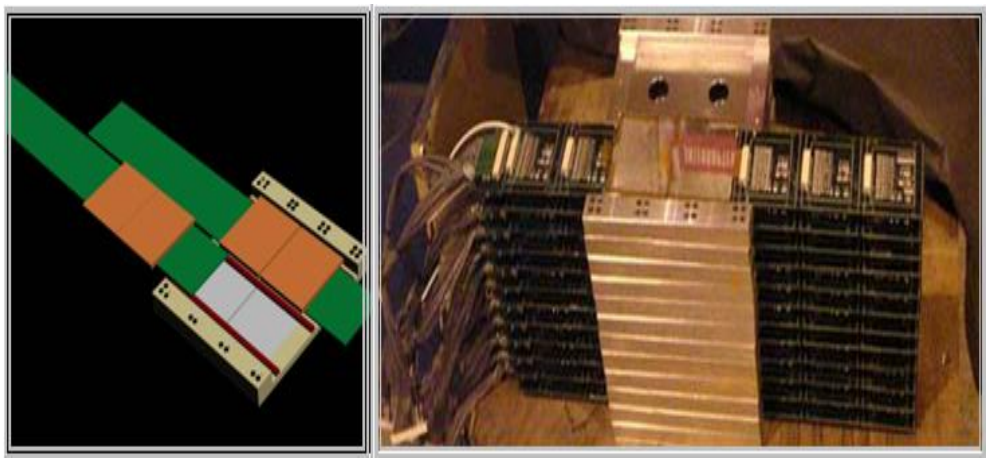

Figure 4.10: The assembly process

In Figure 4.10 each layer has the ability to detect some particles. but we must arrange these in order. To do it we have designed some supporter which

is able to arrange the structure of Figure 4.10. Figure 4.11 and Figure 4.12 show our designs of the supporter. The order of set-up of the supporter is

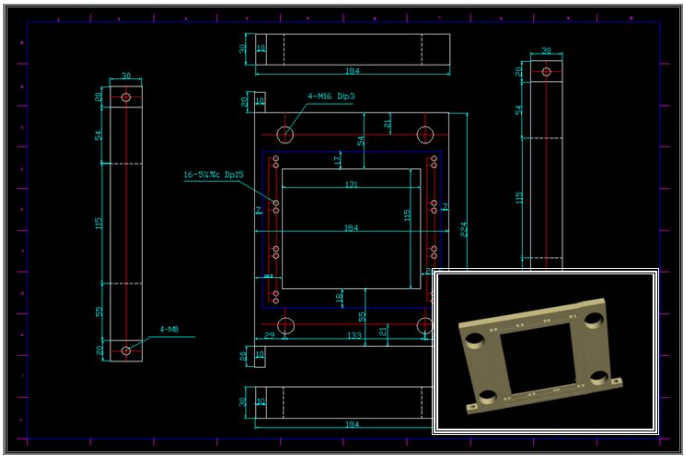

Figure 4.11: The Supporter Type 1

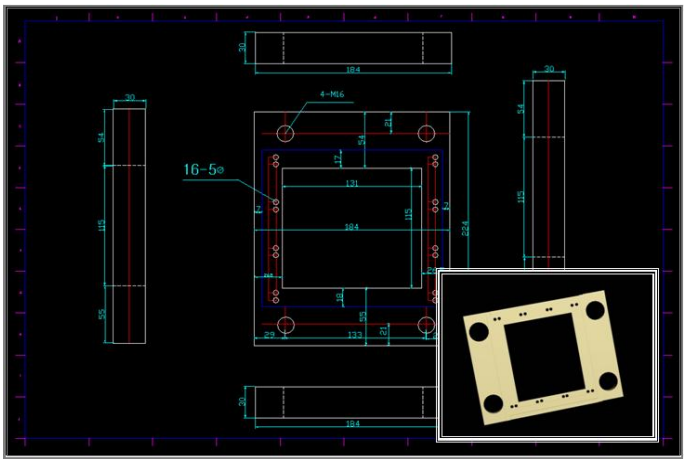

Figure 4.12: The Supporter Type 2

that first, we stand the supporter type 1 and we insert the pole into the hole of the supporter and then each layer assembled files up on the pole. After finishing to accumulate all layer, put on the supporter type 2 to fix the whole system. Figure 4.13 show the calorimeter completed.

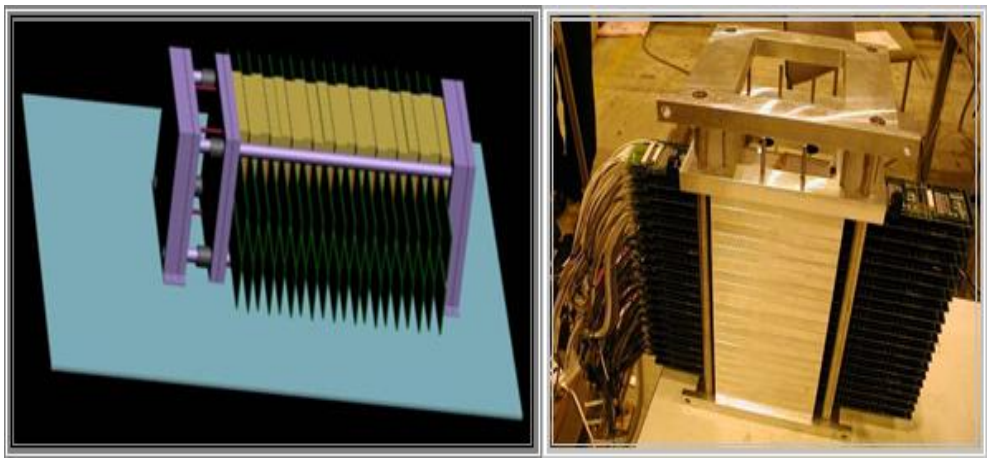

Figure 4.13: The Calorimeter

4.2 Design of the Shielding Box

After the calorimeter has been set up successfully, we need the box which will be able to protect the light and support a heavy structure and place four electronics board(ACP). We have designed that the thickness of the ground, whose material is aluminum,is 10mm and another parts, well and root, are 1mm since the ground is very thick to support the weight. And it has the shelf for setting up of electronic parts. The electronic parts consists of four ACP boards which transfere the analog signals amplified by the analog board into the digital signals.

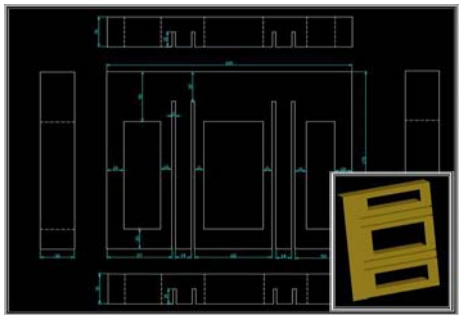

Figure 4.14: The supporter of the shelf

Since the height of our box is not high and four ACP boards had to be entered into the box, we array these up and down each shelf. Therefore we need only two shelfs in the box. We had designed the supporter of the shelf on the condition of the height of two shelfs shown in Figure 4.14. Figure 4.15 is the real shelf picture constructed for the beam test at CERN and the plot plan by MAX.

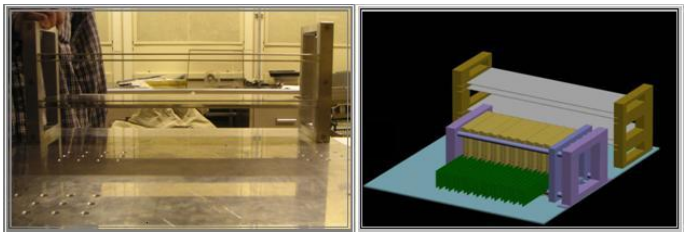

Figure 4.15: The Shelf for the electronics parts

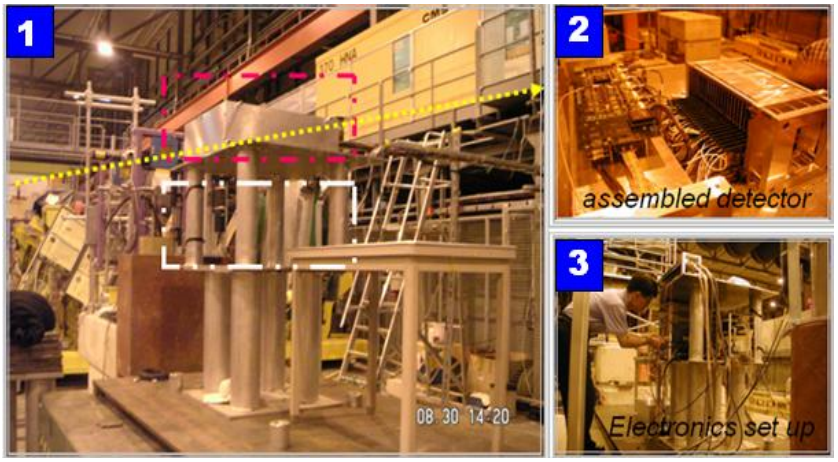

Figure 4.16: The CERN Beam Test space

We must set up the structure completed in the Figure 4.13 on the box. Figure 4.16 illustrates the space for the beam test at CERN. In picture 1, a yellow line is the beam direction. To fix the active area of our calorimeter in the direction of the beam, we have filed up two tables on the lifter. An up-part is the space for the calorimeter and down-part is that for the electronics equipment and remote computer. And a yellow control box, whose we can

see the letter, "CMS" in the wall, is the control room which has a remote control interface that makes us control all the system in our calorimeter from the outside. Picture 2 is the real appearance of the calorimeter set up. Picture 3 is our electronics system set up which has a role to control the ACP boards.

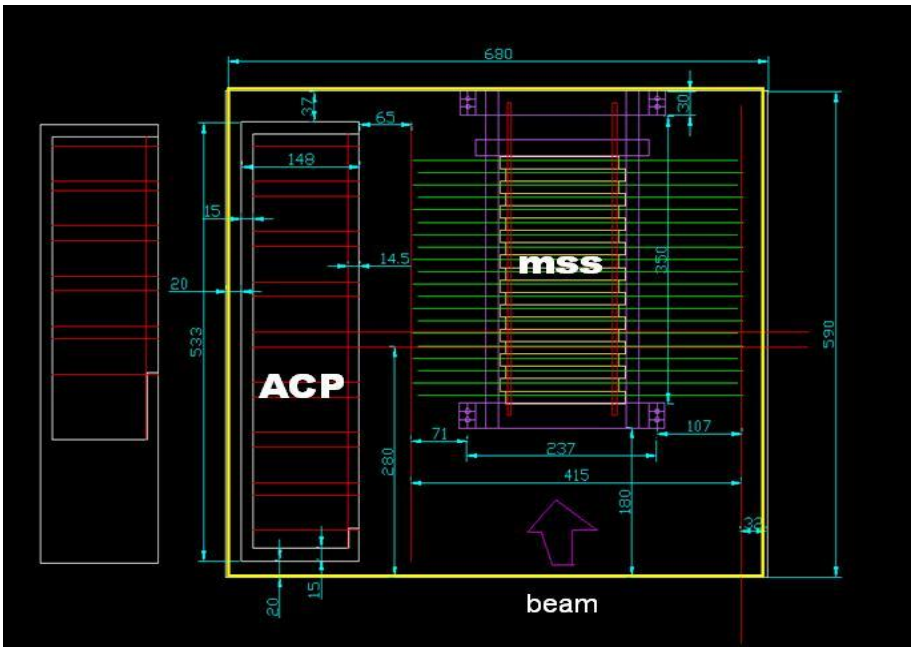

Figure 4.17: An arrangement plan of the calorimeter

In Figure 4.17, we will be able to know the exact position of the detector part and the electronic part. And this figure illustrate 20 layers of our detector. We have the plan to carry out the beam test on 10 layers of our detector. And ACP board has two kinds in the size. so the design of the shelf is two.

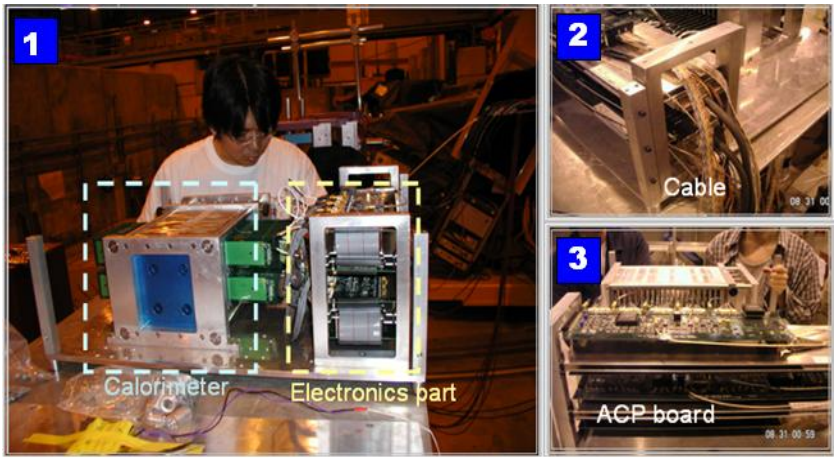

Figure 4.18: The arrangement of the electronics and mechanics parts

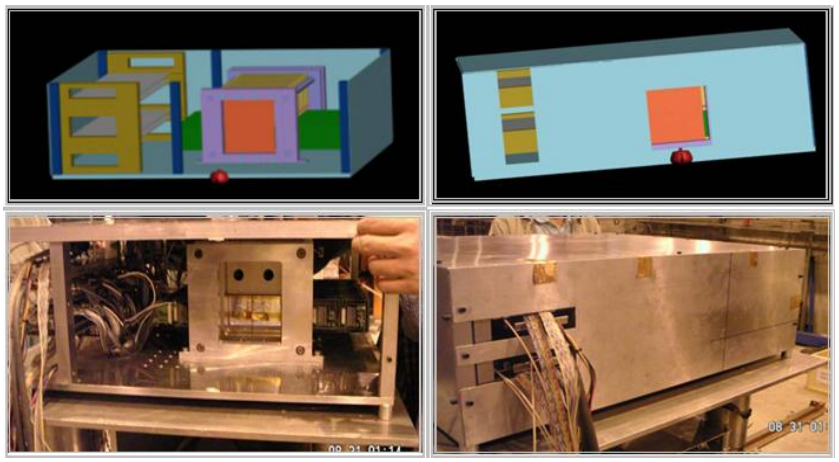

Figure 4.19: The Design of the Box in 3D MAX

In Figure 4.18, Picture 1 is the whole looks of the calorimeter and electronic part which contains the ACP boards. And in Picture 2, all cable of the ACP board direct to the front side so we must make the hole the side of a front. Picture 3 is the real arrangements of ACP board after we set up it totally. And then we must cover the set-up system with the box in the Figure 4.19. In the design of box, we are able to see the front hole for the cable of the ACP board and the point for the beam shooting. Figure 4.20

illustrate the appearance of the beam test in process.

Figure 4.20: The appearance of our CERN Beam Test

4.3 Next Design of Mechanical Structure

In process of beam test, we find a problem about the design of mechanical structure. First, a total assembly time of our calorimeter is about 4 hour. If we find some errors after completing this assembly, we have to take a more time to start the beam test. Second, though we want to do another tests,namely changing the order of layers or replacing a bad sensor with a good sensor, in process of beam test, we are not able to do them since the total assembly time of our calorimeter is very long. So we had necessary of an improvement design after coming back at CERN. New design concept is to make the mechanical structure more manageable. Figure 4.20 illustrates next design of mechanical structure.

Picture 1 is the basic supporter whose material is aluminum. Its character is very thin so the thickness of this structure do not affect total thickness of our detector. We substitute the detector of a layer with the combination of the basic supporter and PCB as showed in Picture 2. And we set up mss and supporters except the part of PCB and sensor in Picture 4. And this role is a

drawer. And we will be able to insert the combination of the basic supporter and PCB in a drawer. And if we have some need to replace sensors, we will be able to do it easily. This is our new idea for the next design of mechanical structure.

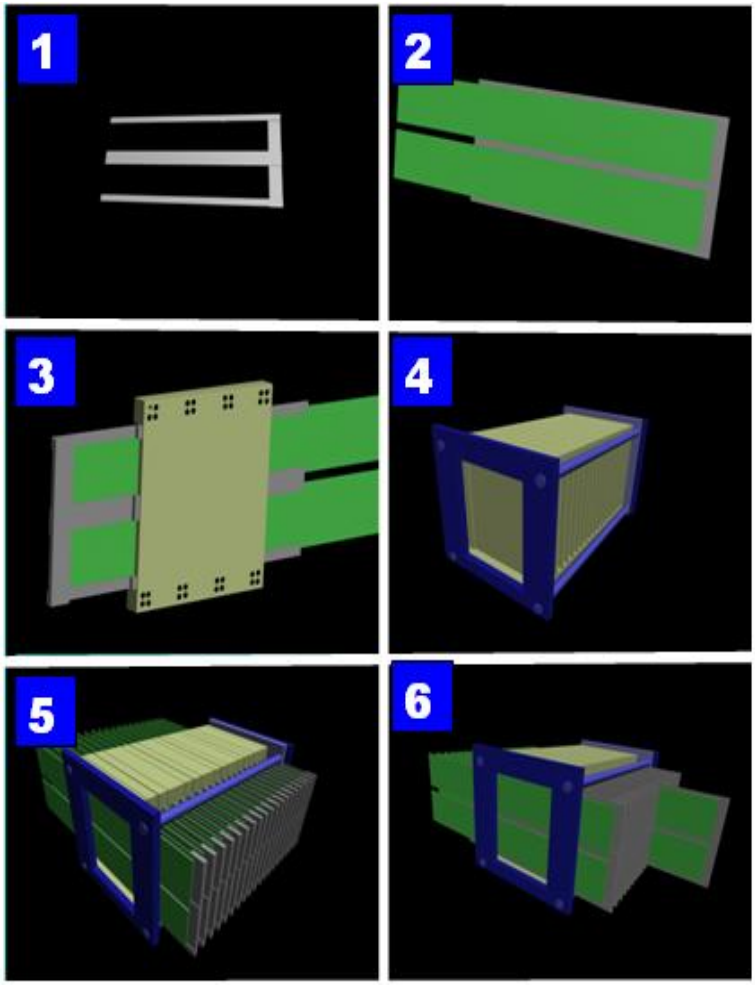

Figure 4.21: Next Design of Mechanical Structure

Chapter 5

Analysis Results

After the beam test at CERN, we have a lot of data files. Total size of a raw data is 51 Gbyte. In order to analysis our beam test result,however we have to transfer our data files into the easily manageable files. And we select the type of ROOT to analyze our data. The size of a processed data which has the type of root files is 7.5 Gbyte. In a processed data, there are totally 861 runs. And the size of each run is 57 Mbyte. From now on, we will explain the structure of our run's data and the process which we develop analysis code for.

5.1 Si-Cal Data Structure

First of all, we look around what kinds of beams we have and which energy we have. Table 5.1 illustrate beam test profile. We have four kinds of the beams; muon, pion, hadron and electron. And the energy level of a muon, pion and hadron is 150 GeV. But the energy level of an electron is 150 GeV, 100 GeV, 80 GeV, 50 GeV, 30 GeV and 20 GeV. Each run has same structure,Namely, they have two root files in common; SiwTree.root and SiwAdcHist.root.

In the SiwTree.root, data is filed up in the form of the Tree structure, which we use when we want to store large quantities of same-class objects. The advantage of the Tree structure is compression,Namely, this can produce

Beam	Energy(GeV)	Layer#	File-num	Comment
muon	150	20	034-056	TD Check
e^-	50	20	057-090	TD Check
pion	150	20	097-137	
muon	150	20	155-196	sensors scan
e^-	150	20	197-285	
e^-	100	20	286-351	
e^-	80	20	352-408	
e^-	50	20	409-450	
e^-	30	20	451-518	
e^-	20	20	529-566	
e^-	10	20	567-608	
hadron	50	10	609-632	
muon	150	10	635-653	
e^-	150	10	654-722	
e^-	100	10	723-770	
e^-	50	10	771-806	
e^-	20	10	807-846	

Table 5.1: 2004 CERN Beam Test Data Sheet

a much smaller file than if the object were written individually. For example, the size of our processed data, 7.5 Gbyte, is less than that of our raw data, 51 Gbyte. The Tree has a parameter which is called a branch. Each branch can be written to separate files. we have two kinds of branches; evt and siw. Figure 5.1 is shown how CERN Beam Test Date is saved.

First branch, evt represents event. When a beam is shot into our calorimeter, our triger begins to work in a moment and ends to work soon. This is one event. In our case, the number of shooting the beam is 5000 for a run. Second branch, siw represents ADC value, which is the unit of the digital signal. And to check the relation between ADC and GeV is one of our experiment goals.

Each run has 5,000 event and each event keep the adc value of 672. So the number of ADC each run is 3360000. There are 672 histogram in the SiwAdcHist.root. each histogram represents ADC values which each channel

had during 5,000 event. Figure 5.2 illustrate the histogram obtained by ADC values which channel 6 had in the case of an electron beam whose energy is 80 GeV.

```
root [10] .ls
TFile**         SiwTree.root
 TFile*         SiwTree.root
  OBJ: TTree    SIWEvent        SIWEvent : 0 at: 0x88f5528
  KEY: TTree    SIWEvent;1      SIWEvent
  KEY: TH1F     hPED;1  PED
  KEY: TH1F     hRMS;1  RMS
root [11] SIWEvent->Print();
*******************************************************************************
*Tree    :SIWEvent  : SIWEvent                                                *
*Entries :     5000 : Total =       13841461 bytes  File  Size =    4987207 *
*       :          : Tree compression factor =   1.00                       *
*******************************************************************************
*Br    0 :ID        : ID/C                                                   *
*Entries :     5000 : Total  Size=      69542 bytes  All baskets in memory   *
*Baskets :        1 : Basket Size=      32000 bytes  Compression=   1.00     *
*.............................................................................*
*Br    1 :evt       : evt/I                                                  *
*Entries :     5000 : Total  Size=      32402 bytes  One basket in memory    *
*Baskets :        0 : Basket Size=      32000 bytes  Compression=   1.00     *
*.............................................................................*
*Br    2 :HeaderTime : HeaderTime/I                                          *
*Entries :     5000 : Total  Size=      32444 bytes  One basket in memory    *
*Baskets :        0 : Basket Size=      32000 bytes  Compression=   1.00     *
*.............................................................................*
*Br    3 :siw       : siw[672]/s                                             *
*Entries :     5000 : Total  Size=   13706788 bytes  All baskets in memory   *
*Baskets :      217 : Basket Size=      32000 bytes  Compression=   1.00     *
*.............................................................................*
```

```
root [4] SIWEvent->Scan()
************************************************************************
*    Row   * Instance *       ID *       evt *  HeaderTim *       siw *
************************************************************************
*      0 *        0 *        0 *         1 *         0 *      4142 *
*      0 *        1 *        0 *         1 *         0 *      4126 *
*      0 *        2 *        0 *         1 *         0 *      4091 *
*      0 *        3 *        0 *         1 *         0 *      4203 *
*      0 *        4 *        0 *         1 *         0 *      4164 *
*      0 *        5 *        0 *         1 *         0 *      4168 *
*      0 *        6 *        0 *         1 *         0 *      4275 *
*      0 *        7 *        0 *         1 *         0 *      4157 *
*      0 *        8 *        0 *         1 *         0 *      4107 *
*      0 *        9 *        0 *         1 *         0 *      4218 *
*      0 *       10 *        0 *         1 *         0 *      4229 *
*      0 *       11 *        0 *         1 *         0 *      4156 *
*      0 *       12 *        0 *         1 *         0 *      4091 *
*      0 *       13 *        0 *         1 *         0 *      4138 *
*      0 *       14 *        0 *         1 *         0 *      4161 *
*      0 *       15 *        0 *         1 *         0 *      4128 *
*      0 *       16 *        0 *         1 *         0 *      4111 *
*      0 *       17 *        0 *         1 *         0 *      4091 *
```

Figure 5.1: SiCal data Tree Structure

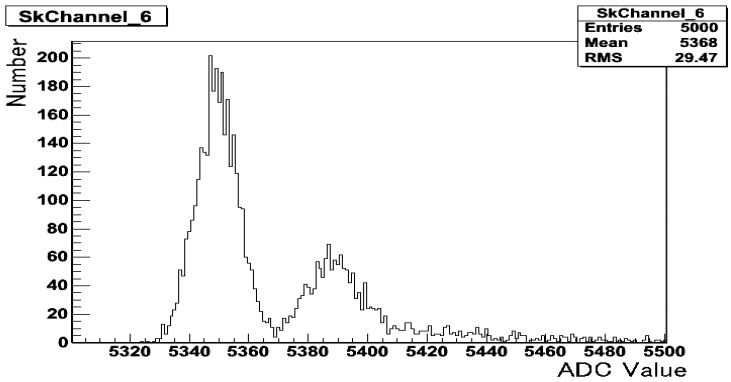

Figure 5.2: Data 360 - Channel 6 histogram

5.2 Data Analysis Code

Information which we will be able to have captured in each run is two fold; the pedestal of each channel and the pure beam data at each run. And by using the pure beam values, we have to make two kinds of histograms; the longitudinal histogram and the transverse histogram. In this chapter, we are to look over the method how we find out the longitudinal and transverse profiles.

5.2.1 a Pedestal

To find a pedestal at each channel we divide our run data into the data by the beam trigger and the data by the random trigger. but we do not clear distribute between them. Since the trigger used at CERN beam test is not subject to our control, its recording do not remaining to us. So we find another method. Above all, we make the histogram which has ADC values of all channel each event. And we can make 5000 histogram as we have 5000 event in each run. Figure 5.3 shows the example of the histogram made by ADC values which event 100 had in the case of electron beam whose energy is 80 GeV.

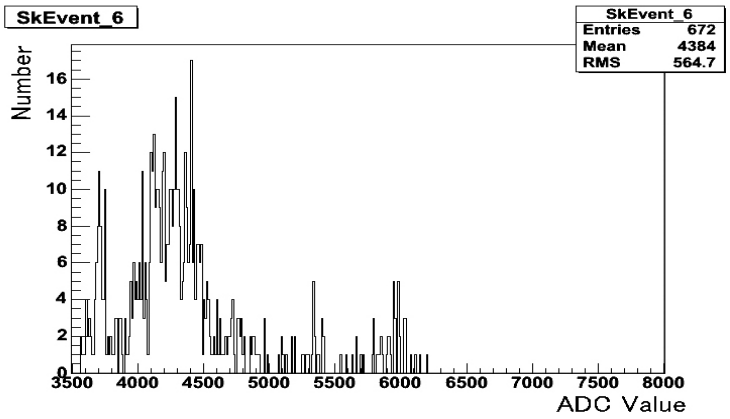

Figure 5.3: Data 360 - event 100 histogram

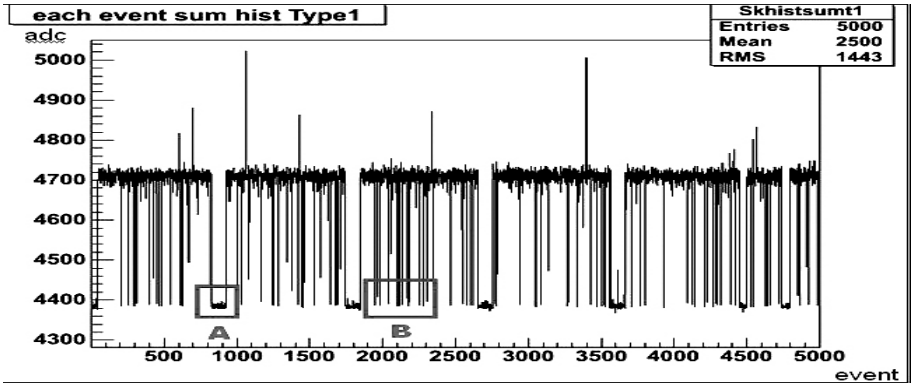

Figure 5.4: The distribution of total energy each event - adc *vs*. event

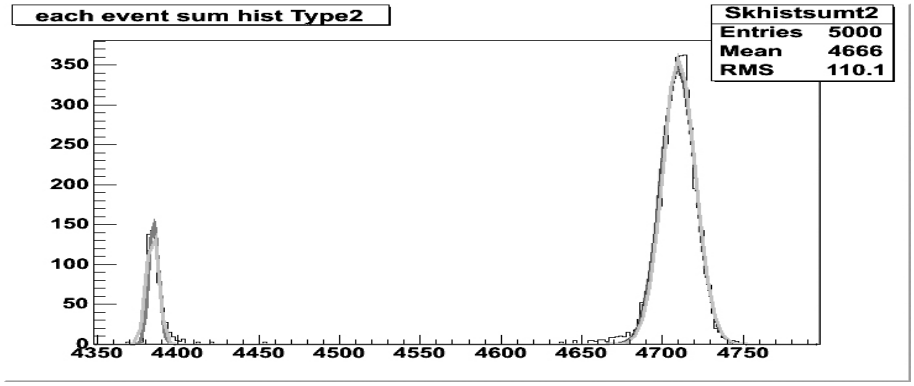

Figure 5.5: The distribution of total energy each event - number *vs*. adc

And then we add up all ADC value in each histogram, which has 672 enteries. So we have total energy value in each event expressed as ADC unit. Because the value is very large, we divide this into 640 to handle easily. Since the number of event in each run is 5000, we are to have 5000 values. Through 5000 ADC values, we are able to make two kinds of histograms; Figure 5.4 and Figure 5.5. In Figure 5.4, we can find some structure; the structure of prominence and depression. In figure 5.5, two histogram separated. At the beam test, we have used two kinds of triggers; a beam trigger and a random trigger. And the random triggers has two kinds; an out-spill random trigger and an in-spill random trigger.

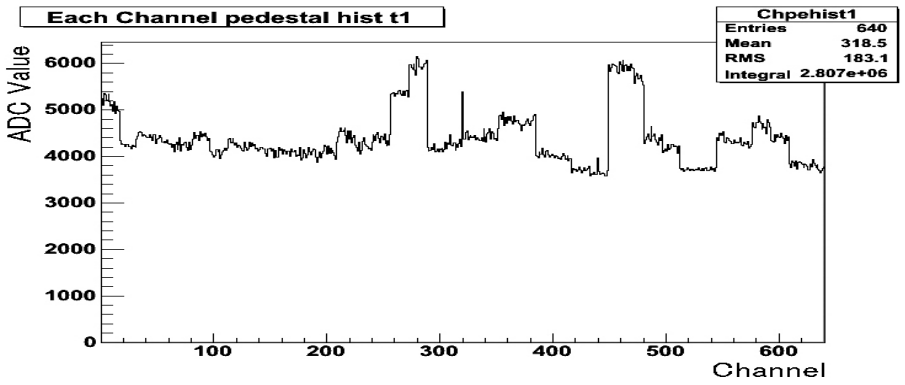

Figure 5.6: The distribution of a pedestal each channel - ADC *vs.* channel

In the case of out-spill, trigger is operated after shooting of the beam. And in the case of in-spill, trigger is operated in the middle of shooting of the beam. Therefore we are to conclude that part A represents an out-spill random trigger and part B represents an in-spill random trigger. In general, we are to take out the pedestal of the system from values of the random trigger. We divide the ADC value into two roughly in Figure 5.4. we can also know this fact definitely in Figure 5.5.

If we decide some standard value to divide events into two, we can think that the event of the value which is less than this standard value is a pedestal events. But the problem is that this way is very subjective since we do not have the definite reason why we select that. This can be a factor of our system error. The standard value of this data is 4440. And we have divided 5000 events into two. So The number of a pedestal events is 654 and the number of a beam events is 4346. And then in 654 pedestal events we have averaged the all ADC values each channel Figure 5.6 is representing the pedestal each channel.

5.2.2 The Longitudinal Profile

In order to generate the longitudinal profile, we have to know the structure of our calorimeter's layers. We have planned for using 21 layers at first. But since the channel whose number is from 128 to 159 had some problems, we except the layer which include the channels of these numbers. So we really had an experiment by using the calorimeter of 20 layers and 640 channels. Figure 5.7 illustrate the real arrangement of our channel, which is a random order. The side number is the layer number. and The upper number is the number of CR chip at the analog board. and we have made our analysis code on the basis of this arrangement.

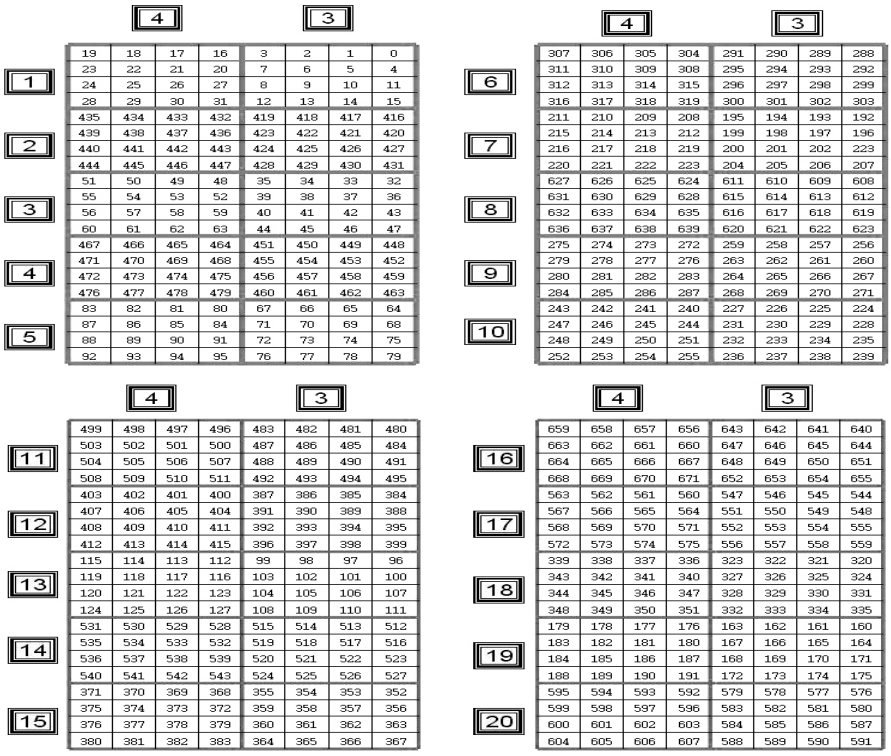

Figure 5.7: The arrangement of a real channel

We want to know an effect of the pedestal at our experiment. So we add up all ADC values each layer of all events including the pedestal events. Through using the arrangement of Figure 5.7, we divide all ADC values into

each layer. And we sum up all ADC in each layer. So we are able to have 20 values. Through using this method, we can make a histogram, like the left side of Figure 5.8. To make the histogram like the right side of Figure 5.8, we have to use the pedestal. We have to select the beam events. In the case of this run(360) data, the number of the beam events is 4346. but if the standard value, 4440 is changed, that will be able to change. And then we subtract the pedestal each channel from ADC value each channel. And then we can take an ADC value of the pure beam. We sum up pure beam data in each layer. So we can have 20 values,too. We can have made another histogram, like the right side of Figure 5.8.

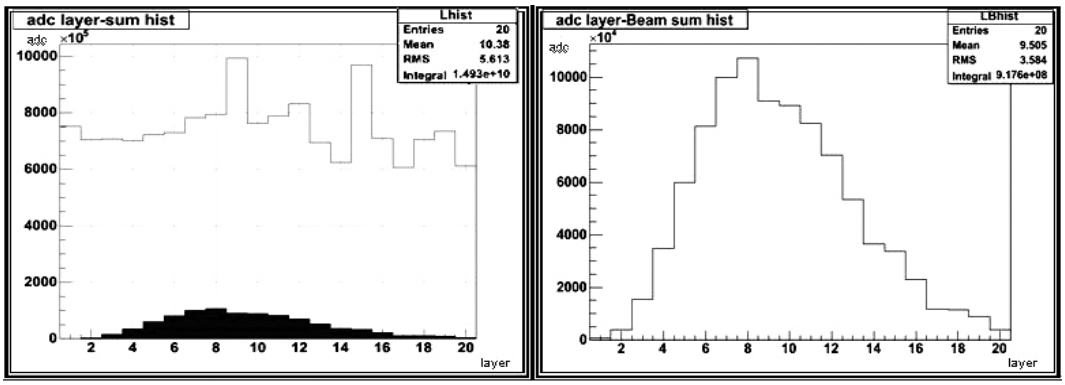

Figure 5.8: The longitudinal Profile

Two histograms are different completely. At the left side of Figure 5.8, we can not find any characters of the longitudinal profiles,namely the effect of the pedestal is very large. In the left side of Figure 5.8, upper line illustrate the histogram both the beam and pedestal and lower line show the histogram of the beam

5.2.3 The Transversal Profile

Figure 5.7 shows the arrangement of channels in each layer is random order. To know exactly the character of the transversal profile, we were to make the method which is to present random arrangement. we manifest this arrangement using array. In the Figure 5.9, we look into the condition of a layer in more detail. we see the analog board which can have seven CR1.4 chip and can set up seven sensor of the silicon.

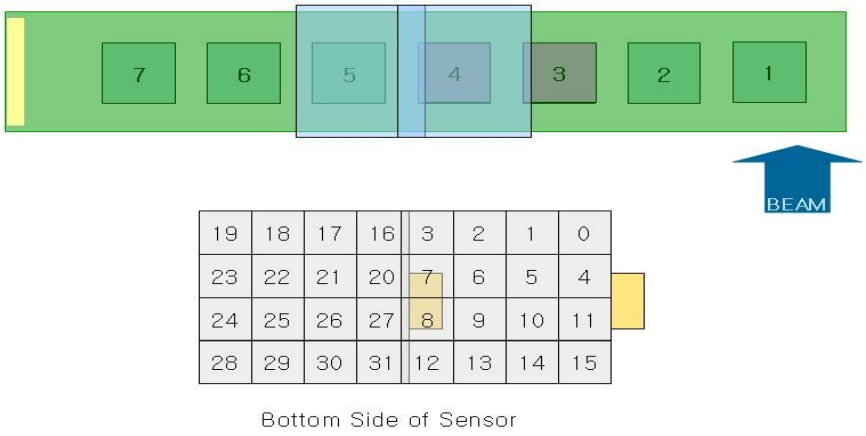

Figure 5.9: The Transversal arrangement of our Calorimeter

The role of a CR1.4 chip is to control and amplify the signal from the silicon sensor. The right side of a sensor is connected by the third CR 1.4 chip and the left side of a sensor is connected by the fourth CR 1.4 chip. In the course of finding the longitudinal profiles, we already have taken 640 ADC total values of the pure beam. Using these values, we can make the histogram of Figure 5.10.

Comparing Figure 5.10 with Figure 5.8, we can know a fact that the outline between both is very similar. And we think that this is very important key point to understand the character of the transversal profile. So we have amplified around channel of the ADC peak values. And we can find the period which is 32 channels,namely, the main part of the shower of electron 80GeV is transferring same position constantly. In order to know the character in

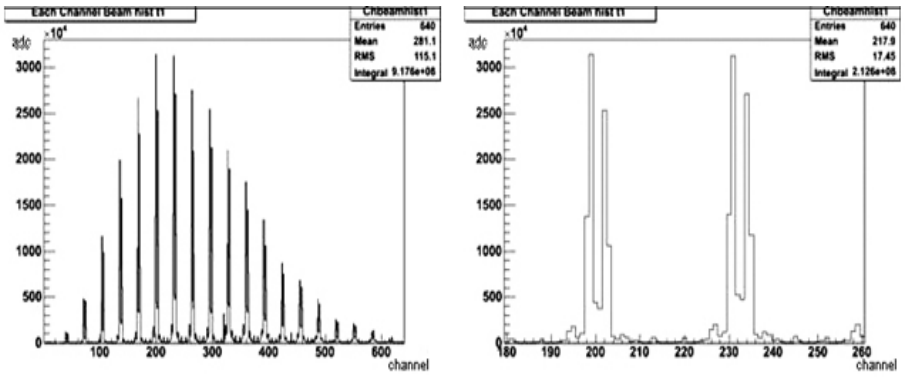

Figure 5.10: The Transversal profile

more detail, we have made 2D-histogram illustrated in Figure 5.11. Figure 5.11 shows 2D-histogram of four kinds about the first layer of the shower of electron 80 GeV. and Figure 5.12 illustrate the transversal profiles for the layers of an odd numbers. We are able to know that the principal part of the electron beam 80 GeV of the data 360 is transferring with the position of channel 6 and 9. And most of beam move into the same position continuously.

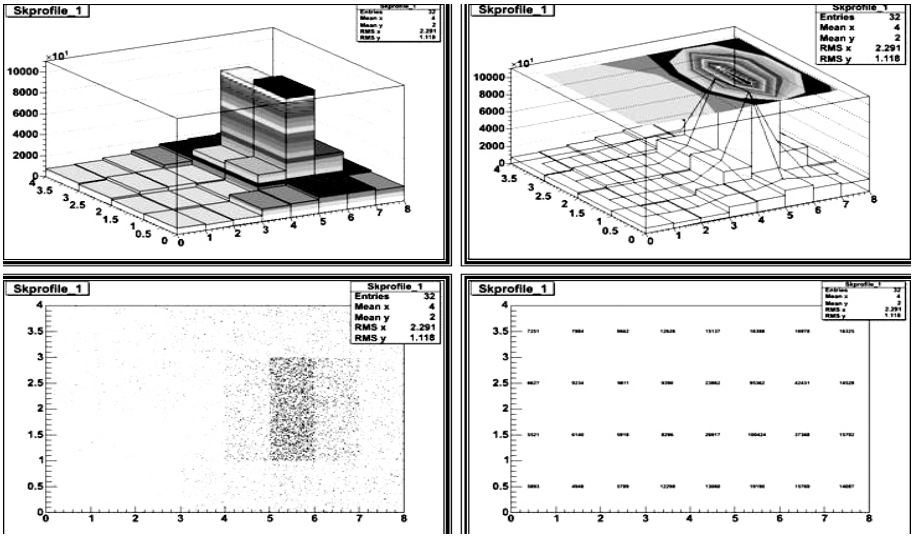

Figure 5.11: 2-D Histogram

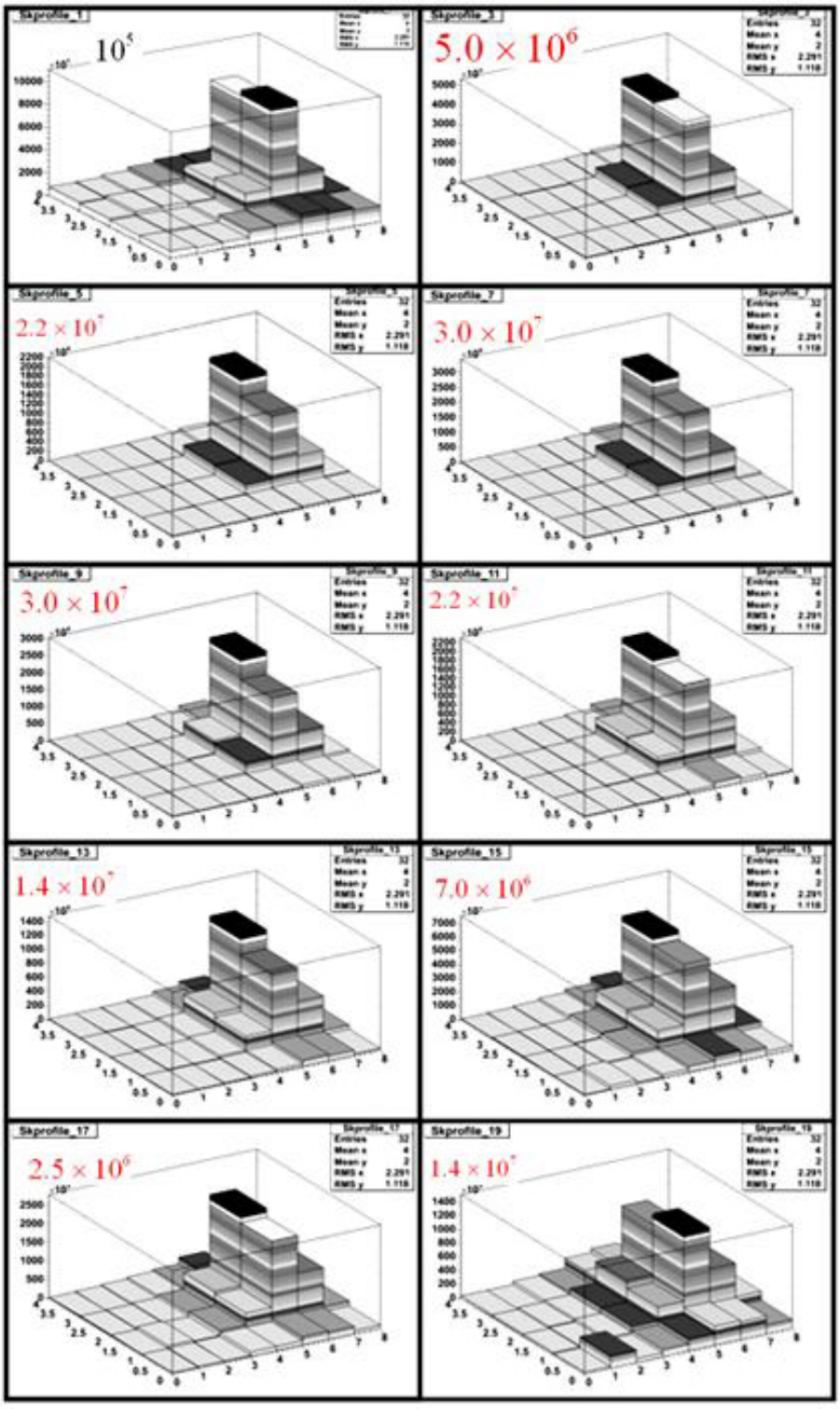

Figure 5.12: The Transversal Profiles

5.3 The Energy Resolution

Until now we have analyzed about data 360; electron 80GeV. But in order to find the energy resolution, we need to have the analysis about more various energy. By Table 5.1 we had the beam test at six kinds of the electron energies. At each energy we will be able to do similar analysis method with the data 360; electron 80GeV. The values which we must find to know the energy resolution is 640 ADC total values of the pure beam.

5.3.1 The Data

We have selected six data files. As the energy is 150 GeV the data number is 198,as 100 GeV the data is 290, as 80GeV the data is 360, as 50 GeV the data is 430, as 30 GeV the data is 460, as 20 GeV the data is 530. Table 5.2 illustrate the character of the data which we have chosen. In the table 5.2, we approximately know the beam position which is the site of the first layer entered into by the beam since the lifter, which supported the calorimeter, was movable slowly. When the energy is changed, the first site is changed too. Then, this fact,lifter is moving automatically, is a fatal problem since we result in an energy resolution under the postulation that the first beam position each energy is same. So we are to find out another method, which we can exactly know the beam position by. And another problem is we can not believe the data of the beam position exactly in the case of 150 GeV and 100 GeV because we don't know the lift can be movable slightly when at these energy we have measured data. But in the case of another data, we can solve this problem by using the method, we reset the position of a lift each run and in the case of the energy of 150 Gev, we select first data, 198.

Data	Energy	Time	Trigger	spill	Beam Position
198	150 GeV	20040902 AM 0:41 0:44	Beam	1402/1402/1124	(254,935.3)
290	100 GeV	20040902 AM 9:24 9:27	Beam and Random	2677/2676/1581	(269.2,935.2)
360	80 GeV	20040902 PM 5:18 5:20	Beam and Random	2046/2046/1616	(263.5,940.1)
430	50 GeV	20040902 PM 11:15 11:18	Beam and Random	2354/2354/1373	(264.6,933.3)
460	30 GeV	20040903 AM 2:00 2:03	Beam and Random	3471/3471/1527	(267,934.1)
530	20 GeV	20040903 AM 9:52 9:54	Beam and Random	5288/5287/1824	(267.9,933.8)

Table 5.2: The Data Profiles.

5.3.2 The Energy Resolution

At first from six data, we must take the ADC values of the pure beam. We can make the histograms each energy by using this data. And then we must fit these histograms by the method of gaussian fitting.

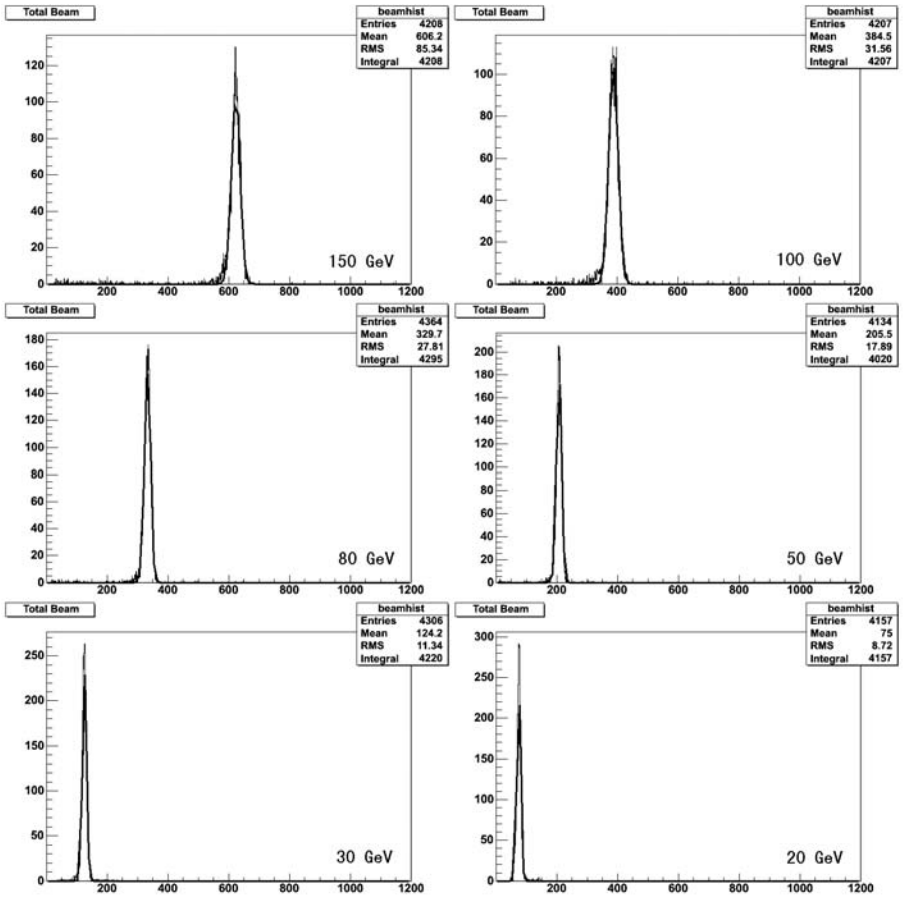

Figure 5.13: The pure beam data in each energy

Figure 5.13 represents the 1D histogram of the pure beam each energy. And these are fitted by the method of the gaussian fitting since the histogram of all natural data is the formaton of the gaussian distribution. The fitting

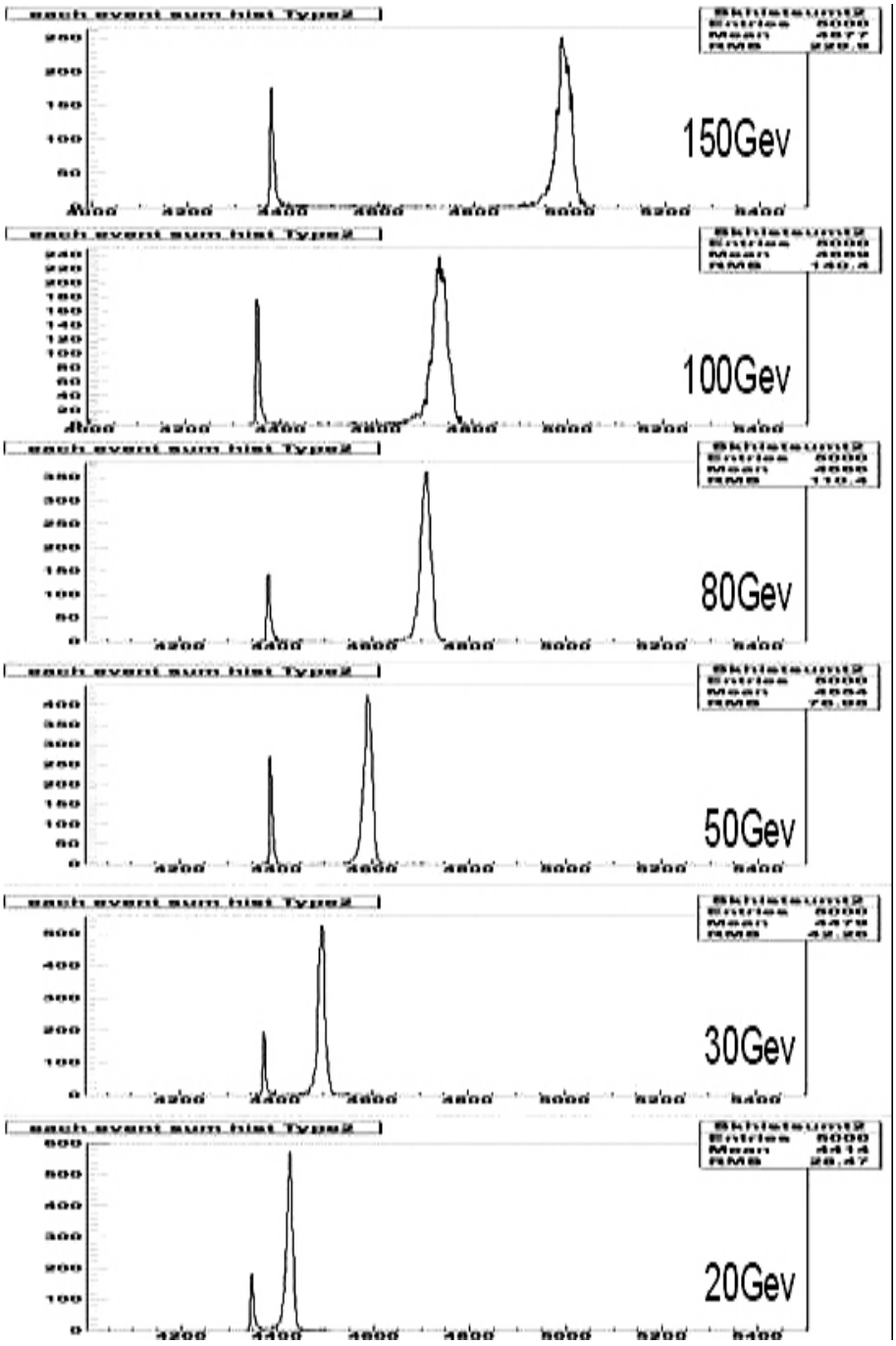

Figure 5.14: Pedestal and Beam each energy

Data	Energy	Constant	Mean	Sigma
198	150 GeV	103.788 ±2.23	623.095 ±0.251	14.577 ±0.206
290	100 GeV	103.877 ±2.13	388.356 ±0.244	15.075 ±0.197
360	80 GeV	163.265 ±3.19	332.328 ±0.159	9.990 ±0.123
430	50 GeV	190.185 ±4.03	206.782 ±0.138	8.013 ±0.109
460	30 GeV	239.217 ±5.08	124.477 ±0.105	6.637 ±0.094
530	20 GeV	255.246 ±5.55	74.905 ±0.103	6.156 ±0.091

Table 5.3: Gaussian Mean and Sigma

values of a mean and sigma each energy, which are the result of the gaussian fitting, represents in the Table 5.3. In Figure 5.13 we can find out that when the energy is decreased, the mean of the graph is moving to the left side,namely, the mean of the histogram is proportioned to each energy. In these histograms, the origin shows the pedestal. In order to know definitely the relative relations between pedestal and beam each energy, we make the histograms which consist of the pedestal and the beam shown in Figure 5.14.

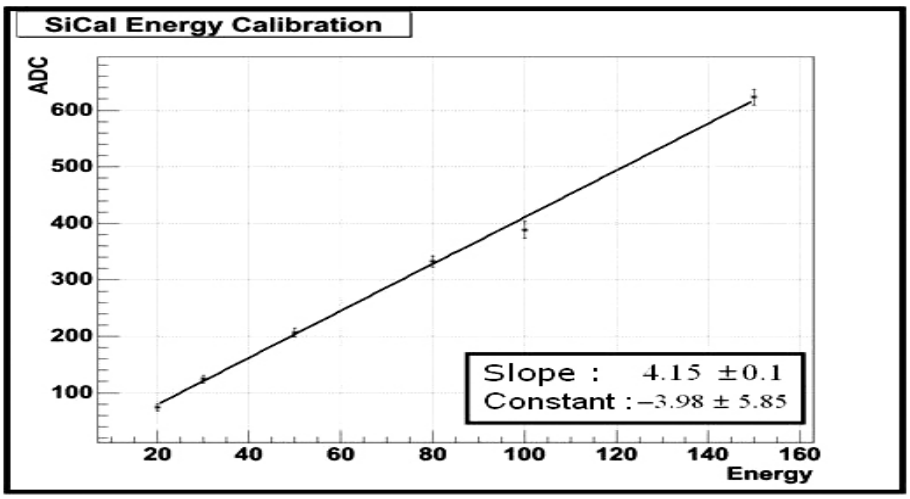

Figure 5.15: The Energy Calibration - ADC *vs.* energy

And we can find an equation about the relation between an ADC values and real energy, namely, we want to know what ADC the energy,1 GeV correspond with. Figure 5.15 shows 1 GeV correspond with 4.15 (± 0.01) ADC. We can transfer all ADC values into the unit of GeV. To find out the Energy Resolution, we must know the sigma value each energy in the unit of energy.

Table 5.4 shows the relation between the sigma in the unit of ADC and that in the unit of GeV.

Energy (GeV)	**Mean (adc)**	**Sigma (adc)**	**Sigma (GeV)**
150 GeV	623.095	14.577 ±0.206	3.512 ±0.050
100 GeV	388.356	15.075 ±0.197	3.633 ±0.047
80 GeV	332.328	9.990 ±0.123	2.706 ±0.030
50 GeV	206.782	8.013 ±0.109	1.931 ±0.026
30 GeV	124.477	6.637 ±0.094	1.600 ±0.023
20 GeV	74.905	6.156 ±0.091	1.483 ±0.022

Table 5.4: The change of the Sigma unit

But in the Table 5.4, the sigma whose energy is 100 GeV is more than that whose energy is 150 GeV. We must find the reason why 100 Gev is different with another data. So now we don't use the data of an energy,100 GeV. In the Figure 5.15, the ADC value whose energy is 100 GeV get out of the fitting line as the same reason.

In order to find out the resolution of the energy , we have to use the following formula.

$$\frac{dE}{E} = \frac{\alpha}{\sqrt{E}} + \beta$$

E is the energy which we have used at our CERN beam test; 20 GeV, 30 GeV, 50 GeV, 80 GeV, 150 GeV. and dE is the sigma which is changed in the unit of energy. Figure 5.16 shows that α is 0.313 ± 0.005 and β is -0.002 ± 0.0007. We don't know definitely the reason that the value of β is negative. But we guess that our ROOT code have some error. And to prove that, we need the simulation which has the same structure with our calorimeter. But Since we can't complete the simulation, we can not apply this in this paper. If we have a test about arbitrary beam, we can know an energy using this equation as we already know the values of α and β.

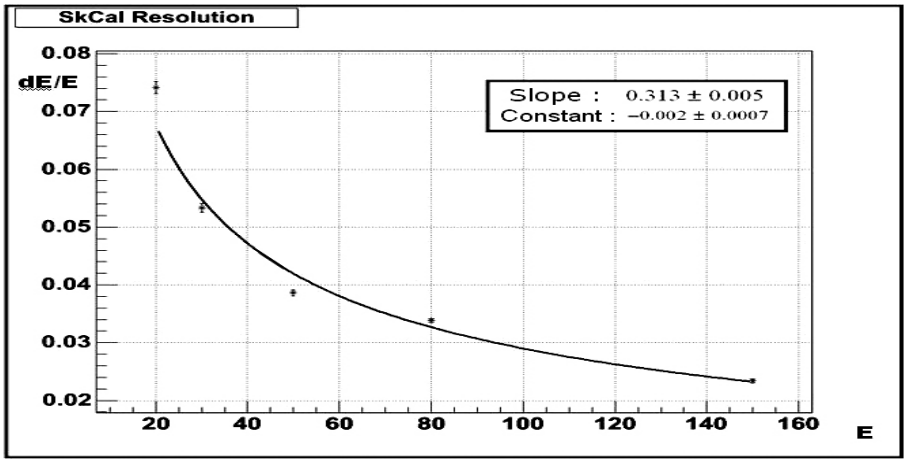

Figure 5.16: The Energy Resolution - Sigma/Energy *vs.* Energy

Chapter 6

Discussion and Conclusion

In this study our purpose is to check our chance to develop an independent technical on calorimeter to be used in ILC. In view of results so far achieved, we succeeded partially in our goal. In short, we will be able to divide the stage of our experiment into three. First stage is to design and make the prototype of a calorimeter by applying the knowhow of the silicon charge detector (SCD), which is a part of the CREAM project[20] and is carried out by Ewha University. Second stage is to carry out a beam test of the prototype at CERN. Third stage is to analyze the data of the beam test at CERN. And we are to finish all stage without mishap. But the result of the data analysis is not better than the criterion suggested by ILC.

Table 6.1 shows the criterion of the detector suggested by ILC. In the case of calorimeter, energy resolution is 15 %. The result of an energy resolution at our calorimeter is 31.3 %. Our result is twice as many as the criterion of ILC. Our Calorimeter is operating but the precision of the data of our calorimeter must be improved. And the thickness of a calorimeter is thicker than the standard of an e^+e^- linear collider. Therefore next prototype must be improved at both the energy resolution and thickness of calorimeter..

Detector	**Configuration**	**Performances**	**Channels and Data Size**
Pair Monitor (3D Active Pixel)	θ = 11 - 48 mrad (r=2 - 8.5 cm) 300 μm-thick × 2 layers pixel size = 100 μm	Under Study	Number of pixels = 8.6M Readout channel = 156ch Data size = 12k bytes/sec
Luminosity Monitor (W/Si)	θ = 50 - 150 mrad 43Xo × 16 samplings N_r = 32, N_ϕ = 16 μm	Under Study	Number of pads = 16.4k Readout channel = 128ch Data size = 3.3k bytes/train
Instrumented Mask (W/Si)	θ = 150 - 200 mrad 23Xo × 8 samplings N_r = 10, N_ϕ = 32 μm	Under Study	Number of pads = 5.1k Readout channel = 16 Data size = 5.1k bytes/train
VTX (CCD)	$cos\theta < 0.90$ pixel size = 25 μm, thickness = 300 μm 4 layers at r = 2.4, 3.6, 4.8, 6.0 cm	σ = 4.0 μm $\delta^2 = 7^2 + (20/p)^2$ / $sin^3\theta$ [μm] ε_b = 50% @ purity = 93%	Number of pixels = 320M Readout channel = 2.4k Data size = 1.4M bytes/train
IT (Double-sided Si-strip)	$cos\theta < 0.90$ strip pitch = 100 μm, thickness = 300 μm 5 layers at r = 9, 16, 23, 30, 37 cm	σ_{rphi} = 40 μm σ_z = 30 μm Tracking Performance Under Study	Number of strips = 1.0M Readout channel = 1.0k Data size = under study
CDC (Mini-jet)	$cos\theta < 0.70$ (full sample) $cos\theta < 0.95$ (1/5 samples) r = 45 - 155 cm, L = 310 cm N_{sample} = 50	$\sigma_{r\phi} \leq 100$ μm σ_z = 1 mm 2-track separation = 2 mm $\sigma_{Pt} = 3 \times 10^{-4} Pt + 0.1$ %	200MHz FADC Memory depth = 10 μsec Readout channel = 4.1k × 2 Data size = 3.3M bytes/train
Trackers-combined		$\sigma_{Pt} = 1 \times 10^{-4} Pt + 0.1$ %	
CAL (Pb/sci-tile/fiber)	EM = 27Xo (3sections) HAD = 6.5λ_o (4sections) $\Delta_{\theta,\phi}$ = 24 mrad(EM), 72 mrad(HAD) $cos\theta < 0.996$ (full thickness) r = 160 - 340 cm, z = ± 190 cm	σ/E = 15 % / $\sqrt{\text{E}}$+1% (EM) σ/E = 40 % / $\sqrt{\text{E}}$+2% (Had) e/π ID = 1/1000	Number of cells = 144k Readout channel = 5k Data size = 3k bytes/train
Shower Position Detector	Two sets of scin.strip (1cm-wide) or Si-pad (1cm × 1cm)	σ = 3 mm / $\sqrt{\text{E}}$	Readout channel = 5k Data size = 40k bytes/train
MUON	$cos\theta$ <0.998, 6 SuperLayers	σ = 0.5 mm	Readout channel = 10k

Table 6.1: Parameters and performance of the ILC detector.

Bibliography

[1] Thomas Hambye and Kurt Riesselmann DESY 97-152 (1997).

[2] M.Tigner, Nuovo Cimento 37, 1228 (1965), U.Amaldi, Phys. Lett. 61B, 313 (1976)

[3] Shingo Kiyoura, Sjinya Kanemura and Kosuke Odagiri, KEK-TH-864 (2003)

[4] T.Tsukamoto, K. Fujii, H. Murayama, M. Yamaguchi and Y. Okada, Phys. Rev. D 51 (1995) 3153

[5] Mariano Quiros, Jose Ramon Espinosa, CERN-TH/98-292 (1998)

[6] Proposal 317 - The CALICE collaboration: calorimeter studies foe a future linear collider (April 29,2002)

[7] Gordon kane, Modern Elementary Particle physics (updated edition)

[8] S.Kanemura, T. kasai, Y.Okada, phys. Lett. B471, 182 (1999)

[9] Y.Okada, M.Yamaguchi, T.Yanagida, Prog. Theor. Phys.85,1(1991), Phys. Lett.B262,54(1991); H.E.Haber, R.Hempfling, Phys. Rev. Lett.66,1815(1991).

[10] T.Moroi, Y.Okada,Phys. Lett. B295,73 (1992)

[11] Richard Wigmans, Calorimetery:Energy Measurement in Particle physics

[12] Y.S. Tsai, Rev. Mod. Phys. 46, 815 (1974)

[13] O.I. Dahl, private communication

[14] Particle Data Group, PHYSICS LETTERS B, 247(15 July 2004)

[15] W.R.Nelson, T.M. Jenkins, R.C. McCall, and J.K. Cobb, Phys. Rev. 149, 201 (1996); G.Bathow et al., Nucl. Phys. B20, 592 (1970)

[16] M.J. Berger and S.M. Seltzer, Tables of Energy losses and Ranges of Electrons and Positrons, National Aeronautics and Space Administration Report NASA-SP-3012 (Washington DC 1964)

[17] Richard Wigmans, Calorimetery: Energy Measurement in Particle physics

[18] G.L.Bashindzhagyzn, N.A.Korotkova, Il H. Park, LCWS 2002, 581 (2002)

[19] Particle Data Group, PHYSICS LETTERS B, 98(15 July 2004)

[20] I.H.Park, H.S. Ahn, NIM A 535 (2004) 158-161